Fe-C nanoparticles obtained from thermal decomposition employing sugars as reducing agents

L. Cervera[1,2], J.I. Peréz-Landazabal[1,2], E. Garaio[1,2], M. Monteserín[3], S. Larumbe[3], F. Martín[3], and C. Gómez-Polo[1,2(*)]

[1]Departamento de Ciencias, Universidad Pública de Navarra, Campus de Arrosadia, 31006 Pamplona, Spain.

[2]Institute for Advanced Materials and Mathematics (INAMAT[2]), Universidad Pública de Navarra, Campus de Arrosadia, 31006, Pamplona, Spain.

[3]Surface Engineering, Asociación de la Industria Navarra, 31191 Cordobilla, Navarra, Spain.

Abstract.- The aim of the work is to present a comparative analysis (structural and magnetic) of Fe-C nanocomposites obtained by the thermal decomposition of sugars (fructose, glucose and sucrose) employing $FeCl_3$ as Fe^{3+} precursor. The thermal decomposition was followed through Thermogravimetry (TGA) and Fourier-transform infrared spectroscopy (FTIR), X-ray diffraction, High Resolution Transmission Microscopy (HRTEM) and Raman spectroscopy. The results indicate the reduction of Fe^{3+} under the performed thermal treatments and the achievement at high annealing temperatures of Fe-C nanostructures (coexistence of α-Fe and Fe_3C nanoparticles surrounded by a carbon matrix). The magnetic characterization performed by *dc* SQUID magnetometry, shows an antiferromagnetic response in the initial stages of the decomposition process, and a ferromagnetic behavior linked to the Fe-based nanoparticles. The magnetic induction heating was analyzed through the *ac* hysteresis loops. Moderate Specific Absorption Rate (*SAR*) is obtained in Fe-C nanoparticles ($\sim$ 70 W/g_{Fe}), ascribed to the large nanoparticle size. The combination of porous carbon structure and ferromagnetic response of the Fe-C nanoparticles

(i.e. local temperature increase under *ac* magnetic field) enlarge the emerging applications of these carbonaceous nanocomposites.

(*) Corresponding autor.-
Prof. Cristina Gómez-Polo
Departamento de Ciencias. Edificio de los Acebos.
Universidad Pública de Navarra. Campus de Arrosadia. 31006 Pamplona. Spain
Phone. +34-948169576; e.mail: gpolo@unavarra.es

1.- Introduction

Functional nanostructured carbon materials have drawn a great attention in the last decade due their potential use in different technological and industrial fields: energy related applications [1] (supercapacitors [2], fuel cells [3] and batteries [4]); electrochemical sensors [5]; chemical adsorbents [6] and catalysts [7]; or electromagnetic shielding elements [8]. Their multifunctional response is based on the specific surface characteristics, such as high surface area and porosity that enables them to be functionalized by other active functional systems. Among them, the inclusion of metal transition elements (i.e. Fe, Co, Mn, Cu) stands out [9-12], included as anchored cations in the carbonaceous nanostructure or as individual nanoparticles forming hybrid nanostructures.

In particular, Fe based carbonaceous nanocomposites represent a very active current research topic due to its applications in different emerging fields such as environmental applications (namely, removal of pollutants) [13, 14], electrochemical sensing [15], catalysis [16, 17], energy applications [18, 19], biomedical field [20, 21] and electromagnetic absorption [22, 23]. These materials show a synergic effect between the contribution of Fe atoms in the carbon nanostructure and the magnetic contribution inherent of iron based compounds.

Nevertheless, in most of these analyzed nanocomposites, Fe is synthesized in its oxidized form, mainly as ferrimagnetic (magnetite Fe_3O_4, maghemite γ-Fe_2O_3) or antiferromagnetic (α-Fe_2O_3) phases. However, carbonaceous nanocomposites containing metallic (zero-valent) Fe have been widely explored mainly in the environmental field for waste water and soil remediation [24, 25]. In fact, nanoscale zero-valent iron, Fe^0, (nZVI) is a strong reducing agent that has been extensively proposed for the reduction of toxic metal

ions (Cr(VI) [26], Cu(II) [27] or Zn, Pb and Cd [28]) or nanocatalysts [29]. In this nanocomposites, the reducing activity of the Fe^0 is reinforced by the adsorption properties of carbon based support nanostructures (i.e. activated carbon (AC) [30], graphene oxide (GO) [31] and carbon nanotubes (CNTs) [32]). These supports play a double role; on one side, preventing Fe oxidation before the reduction process and guaranteeing the proper dispersion and isolation of Fe^0 within the carbonaceous support; secondly, the high surface area and porosity should enable the interaction with the chemical target element. Furthermore, the magnetic nature of Fe aggregates (high magnetic susceptibility and saturation magnetization) provides the facility of easy separation under the action an external magnetic. However, strong magnetic forces between the Fe^0 aggregates could also represent a drawback of these nanostructures, leading to particle agglomeration and a reduction on their reactivity. Thus, the exploration of versatile synthesis procedures, guaranteeing a homogenous nanosized Fe^0 distribution on the carbon based support, constitutes an important factor in the development of this type of nanostructures. Among them, green synthesis procedures should be highlighted, due to their reduced generated waste and the implementation of cost-effective sustainable processes: hydrothermal [33] and pyrolysis [34] treatments of carbon based organic molecules and materials such as sugars [26, 35] and biomass or biochars [36-39] impregnated by Fe salts. Therefore, reduction of iron carbon nanostructures constitutes the basis of most of the employed synthesis processes, where the reaction parameters such as temperature and duration of the thermal treatment, Fe and C precursors (type and relative amount) are the main factors controlling the final microstructure of the nano/micro composite.

On the other side, these Fe-C nanostructures have been also proposed as multifunctional systems for biomedical applications [20, 21, 40]. Magnetic multifunctional

4

nanoparticles have been extensively analyzed as targeted drug delivery agents, in magnetic hyperthermia therapy and imaging diagnostic procedures [41-43]. In particular, ferrimagnetic iron oxides are preferentially chosen for these applications due to their low toxicity, the possibility to produce them in different shapes and sizes through simple synthesis techniques, and their optimum magnetic response (i.e. superparamagnetism) for biocompatible nanoparticle sizes, among others [44 - 46]. In spite of the reduced toxicity, the introduction of biocompatible coatings is compulsory to provide them the required multifunctionality through the link on the nanoparticle surface of the proper ligands, antibodies, or proteins [47 - 49]. Comparing Fe^0 (metallic or α-Fe) with ferrimagnetic iron oxide based nanoparticles, the reduced iron state gives rise to an improvement on the magnetic response as a consequence of the intrinsic higher saturation magnetization (220 emu/g for α-Fe [50] versus 92 emu/g for Fe_3O_4 [51]). Again, carbon coating appears as the most efficient strategy to obtain stable core-shell metallic Fe based nanoparticles and different synthesis approaches have been reported (i.e. arc discharge, pulsed plasma or high pressure plasma deposition [52-54]). Nevertheless, simple chemical routes and green thermal decomposition of carbon based organic materials have been also explored [55, 56]. An in-depth analysis of the magnetic phases obtained in these nanocomposites shows the coexistence of α-Fe and Fe_3C (cementite) phase [57, 58]. In fact, iron carbides are attractive for biomedical applications since they combine chemical stability with high magnetization (140 emu/g for Fe_3C [59]). Anyway, the toxicity of both Fe·C nanoparticles and carbon coatings should be analyzed and explored to evaluate the application of these nanosystems in the biomedical field.

Focusing on magnetic hyperthermia of nanosized magnetic materials, although it has been extensively analyzed linked to the biomedical field, its application in other

technological areas is currently and actively explored. In particular, the temperature increase under the action of an *ac* magnetic field (magnetic induction heating) has been proposed as Magnetic Induction Swing Adsorption (MISA) systems (controlled gas capture and release) [60, 61]; new synthesis procedures of nanostructures [62, 63]; mechanical recovery or self-healing in polymers and glasses [64-68]; thermoplastic adhesives for bonded joints [69, 70]. Regarding the environmental field, the local temperature increase associated to the *ac* magnetization process of nanosized ferro or ferrimagnetic elements, has been proposed as an effective procedure to activate heterogeneous catalytic reactions [71- 75] and to optimize magnetic adsorbents in wastewater treatments [76].

Accordingly, in this work we present a comparative analysis of Fe based carbonaceous nanomaterials obtained by the thermal decomposition of sugars (fructose, glucose and sucrose) employing $FeCl_3 \bullet 6H_2O$ as Fe^{3+} source. In spite of the extensive reported studies employing similar synthesis procedures, few reports analyze in detail the evolution of the reduction process through a comparative analysis of the magnetic response of the samples. The reduction of Fe^{3+} with the carbonaceous matrix gives rise at the final stages of the decomposition process to the coexistence of Fe-based (α-Fe and Fe_3C) nanoparticles surrounded by the carbon (graphitic) coatings. Particularly, *ac* hysteresis loops and the Specific Absorption Rate (*SAR*) coefficient were analyzed to estimate the capability of these Fe-C nanoparticles as local heating elements. The results indicate that these carbonaceous nanocomposites display the optimum features to be used in a wide range of emerging applications, ranging from environmental applications as magnetic adsorbers and catalysts, electromagnetic absorbers or nanocomposites for the biomedical field.

2.- Experimental procedure

Different sugars (sucrose, fructose and glucose), employed as carbon source, were mixed with an aqueous solution of $FeCl_3 \cdot 6H_2O$ (8 wt. %Fe). The solution was heated at 180 ^0C and stirred until water evaporation to obtain a dark paste. The dried samples will be denoted as P-*sugar* (P-fructose, P-glucose and P-sucrose). This paste was annealed at different temperatures (from 400 to 800 ^0C) during 1h in a furnace under Ar atmosphere in order to prevent iron oxidation. The samples in the annealed state will be denoted as A-*sugar-annealing temperature* (i.e. A-fructose400) for distinguishing them from the initial sugars or the previous dried state.

Firstly, the thermal decomposition of the different sugars and the P-*sugar* samples was followed by Thermogravimetric (TGA) Analysis, (HI-RES 2950 TA Instruments) employing a heating rate of 10°C/min under nitrogen atmosphere. The evolution of the samples in the annealed state was analyzed by Fourier-Transform Infrared spectroscopy (FTIR) using KBr as the window material used in pellets. Regarding the structural analysis of the annealed samples, X-ray powder diffractometry (Siemens D-5000) with monochromated Cu Kα1 radiation (λ= 1.54056 Å) were employed, using Rietveld method and the Fullprof [77] program in the analysis of the spectra. Transmission Electron Microscopy (HRTEM) and Scanning Transmission Electron microscopy with a high angle annular dark field detector (STEM-HAADF) analysis were performed by using a FEI Tecnai Field Emission Gun operated at 300 kV. Raman spectroscopy (Jasco NRS-3100 dispersive Raman spectrophotometer using a 532 nm laser (7mW) and a 600 line grating covering the range 260-3900 cm^{-1}) was employed to analyze the evolution of the carbon in the annealed samples. Powder samples, without further preparation, were exposed 0.1 sec per scan and at least 500 scans were accumulated in order to get a good signal to noise ratio. Finally, the

magnetic characterization of the annealed samples was performed through a SQUID magnetometer (Quantum Design MPMS XL7) and a home-made *ac* magnetometer in the characterization of the *ac* hysteresis loops. The characteristic *SAR* that is, magnetic losses per unit of sample mass or in other words, the heating capacity of the sample, was estimated though the area of the ac hysteresis loop:

$$SAR = -\mu_0 \oint M_t dH_{ac} \tag{1}$$

where M_t is the time dependent dynamic magnetization (normalized by sample mass) and H_{ac} is the externally applied magnetic field intensity. A resonant LCC circuit fed by an *RF* power amplifier (Electronic & Innovation, mod. 1240 L) generated the external magnetic field while the dynamic M_t magnetization was measured by a *ac* magnetometry pick-up coil system previously described in the literature [78].

3.- Results and discussion

3.1. Decomposition analysis

Firstly, TGA analysis was used to obtain structural information about the thermal decomposition of the different employed sugars. Fig. 1 shows the weight loss (%) as a function of temperature for (a) fructose, (b) glucose and (c) sucrose (lines). Comparatively, the thermal decomposition of the dried sugar pastes with Fe^{3+} (P-*sugar*) is also shown (symbols). The thermograph of the initial sugars mainly consists of two main steps at T_1 and T_2, clearly visible through the derivative of the TGA scans (see fig. 1d). Table I summarizes the estimated temperature peak values for the three analyzed sugars.
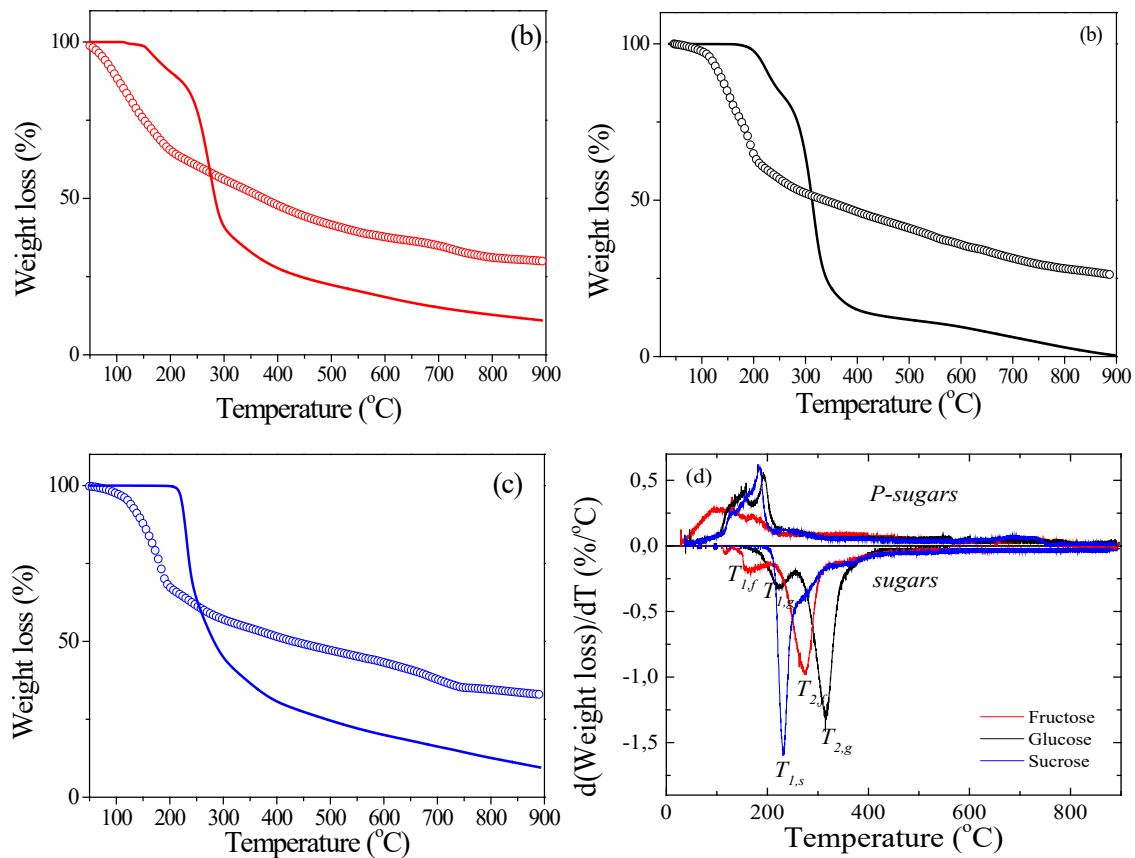
Fig. 1: TGAs curves for the initial sugars (lines) and the P-*sugars* (symbols) for (a) fructose, (b) glucose and (c) sucrose; (d) derivative of the TGA curve (P-*sugars* in absolute value).

As previously reported [79], the occurrence of two decomposition temperatures (T_1 and T_2) are usually associated to melting and final decomposition processes, respectively. Although, a certain variability is found in the reported melting temperatures of the analyzed sugars, a general trend is reported: T_1 (sucrose) > T_1 (glucose) > T_1 (fructose) [80]. In fact, a similar trend is deduced from table I with peak temperature values within the range of the reported melting temperatures in these sugars. The absence of noticeable weight losses around 100°C (flat response for temperatures below 150°C) would indicate a negligible

contribution of water evaporation (moisture). In the case of the sucrose, it is not possible to clearly determine T_2 temperature, being the decomposition process characterized by a single sharp decrease in the weight loss around $T \approx T_1$.

Table I: Decomposition peak temperatures for the analyzed sugars.

sugar	T_1 (°C)	T_2 (°C)	sample	T_1 (°C)	T_2 (°C)
fructose	150	273	P-fructose	--	--
glucose	220	315	P-glucose	150	192
sucrose	231	--	P-sucrose	185	--

Regarding the dried P-*sugars*, a clear shift of the decomposition process towards lower temperatures is obtained in comparison with the initial sugars. This effect, again clearly visible though the weight loss derivative (see fig. 1d, in absolute values), should be mainly interpreted as the catalytic effect of iron in graphitizing carbon materials [81]. Furthermore, these dried P-*sugars* display an initial sharp weight loss for $T \leq 200$°C ascribed to the sugar decomposition, followed by a smooth decrease up to a maximum value around 30% (corresponding to the precipitation of the Fe based nanoparticles). While two decomposition peaks at low temperature on the P-glucose sample can be easily identified, in P-sucrose only a decomposition peak is again clearly visible (table I). The different thermal decomposition in the P-fructose sample for $T \leq 200$°C (broader weight loss peak) should be ascribed to the previous drying procedure at 180°C (notice that the melting temperature of the initial sugar is $T_1 = 150$°C).
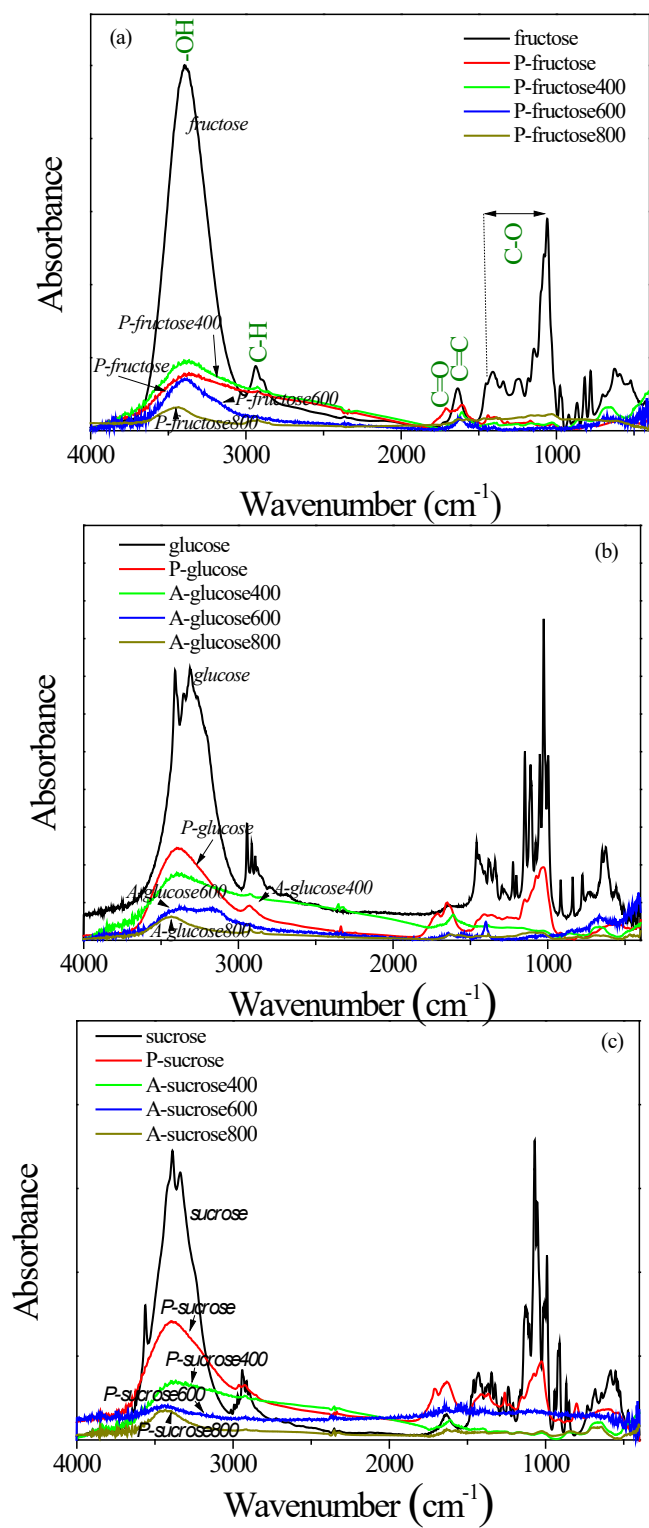
Fig. 2: Comparative evolution of the FTIR spectra for the initial sugars, P-sugars and annealed samples (A-sugars) for (a) fructose, (b) glucose and (c) sucrose.

The comparative evolution of the decomposition process in the samples was additionally followed by FTIR infrared spectroscopy. Fig. 2 displays the FTIR spectra for the initial sugars, P-*sugars* and those reduced at different annealing temperatures (A-*sugar*): (a) fructose, (b) glucose and (c) sucrose. The initial sugars display the characteristic C, H and O functional groups: -OH at 3400-3300 cm^{-1}; C-H at 2900 cm^{-1}; C=O at 1730 cm^{-1}; C=C (aromatics) at 1621 cm^{-1}; C-O (carboxy) at 1403 cm^{-1}; C-O (epoxy) at 1227 cm^{-1}; C-O (alkoxy) at 1061 cm^{-1} [82, 83]. The occurrence of Fe-O cannot be visualized (580 cm^{-1} for magnetite Fe$_3$O4 and 630 cm^{-1} for γ-Fe$_2$O$_3$ maghemite) [84].

As expected, the P-*sugar* samples (dried sugar paste) show a remarkable reduction in the –OH stretching mode as a consequence of the dehydration upon heating (180°C). The carbohydrate bands (between 1000 and 1800 cm^{-1}) also undergo a significant reduction in the initial dried state, further reduced with the increase in the annealing temperature (T_{ann}). As a general trend, a progressive reduction in the organic bands contribution is found as the annealing temperature increases. In fact, a nearly flat FTIR spectra for T_{ann} = 800°C is found in all the annealed samples, where the occurrence of Fe-O stretching modes cannot be completely excluded for high temperature annealing states. It should be noted the occurrence of a shift of the decomposition process towards low annealing temperatures in the sucrose samples). While C=C and C-O modes can be detected in A-fructose600 and A-glucose600 samples, a flat FTIR spectra without clear absorbance peaks is obtained for the A-sucrose600 sample.

3.2. Structural characterization

Regarding the structural characterization of the annealed samples, the X-ray diffraction patterns show for low temperature annealing ($T_{ann} \leq 600°C$ for A-fructos*e* and A-glucose; $T_{ann} = 400°C$ for A-sucrose) a complex phase distribution that cannot be clearly identified to the corresponding crystallized sugars and/or common Fe hydroxides (goethite, lepidocrocite or akaganeite). Nevertheless, a small fraction of Fe_3O_4 (magnetite) phase can be inferred at the beginning of the reduction process for the fructose and glucose samples annealed at 400°C. High temperature annealing ($T_{ann} = 800°C$) leads to the coexistence of α-Fe, Fe_3C and C (graphite) in the three samples (see fig. 3a-c). This phase distribution has been widely reported in Fe-C nanostructures obtained through similar synthesis procedures [85, 86]. Fig. 3 also includes the Rietveld refinement, taking into account the following phases: cementite (Fe_3C) with P*nma* space group (COD 9012188), α-Fe with I*m3m* space group and graphite, with hexagonal Space Group $P6_3mc$. In the case of the sample reduced with sucrose at $T_{ann} = 800°C$, a small fraction of magnetite (Fe_3O_4) with F*d-3m* space group is also obtained. As fig. 3d displays cementite (Fe_3C) is already detected in the pattern of P-sucrose600, supporting the shift of the decomposition process towards lower annealing temperatures in the sucrose samples. Table II summarizes the obtained fitted parameters through Rietveld refinement. It should be noted that all the annealed samples at high temperatures (including A-Sucrose600, fig. 3d) display a majority carbon base phase (75-89 wt %) fitted to the hexagonal graphite phase with lattice parameters similar to those reported in the literature ($a = b = 2.470$ Å, $c = 6.790$ Å, with carbon atoms at 2a(000) and 2b (1/3 2/3 0.005)) [87]. The wide (002) reflection at 25.57 ° in the sucrose annealed at 600 ºC (see fig. 3d) indicates the highly disordered (amorphous) feature of the graphitic phase in this sample.

Thus, the sharp reduction in the (002) peak width clearly indicates the ordering of the carbon phase at higher annealing temperature (i.e. see fig. 3c). Nevertheless, the contribution to this peak intensity of ordered graphitic layers (graphene stack layers) cannot be excluded.

Similarly, for the Fe-based phases, the lattice parameters are within the reported values of the cementite and bcc Fe phases (Fe_3C: $a = 5.089(6)$ Å, $b = 6.744(3)$ Å, $c = 4.524(8)$ Å [88] and α-Fe: $a = b = c = 2.8662(1)$ Å [89], respectively). In all these samples, orthorhombic cementite (Fe_3C) is detected as the majority Fe-based phase (11-22 wt %) and main grain sizes in the range of tens of nm (16-41 nm). Furthermore, a small fraction of α-Fe phase is also detected with larger crystalline grains in the range of hundreds of nm (except the A-glucose800 sample, where $d(\alpha\text{-Fe}) \approx 60$ nm). Surprisingly, a decrease in $wt\%$ for the Fe based phases with respect to the carbon content estimation is found in A-sucrose800 when comparing with the Fe-based phase distribution of the sucrose sample annealed at 600°C. This results could be indicative of the occurrence of other Fe phases undetectable through the X-ray diffraction patterns (i.e. fcc-Fe) as would be discussed linked to the magnetic characterization (section 3.3.a).
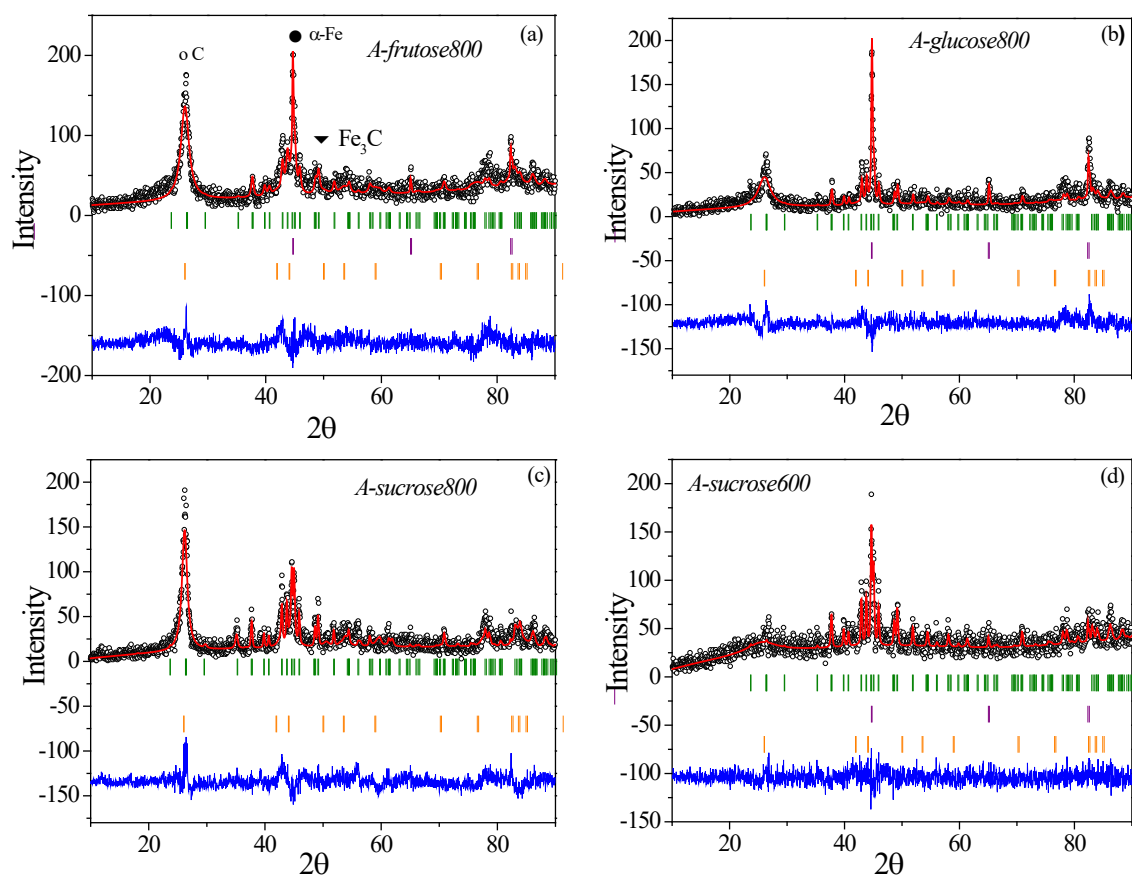
Fig. 3: Room temperature X-ray powder diffraction patters for annealed samples at 800°C (a) fructose, (b) glucose, (c) sucrose and (d) fructose at 600°C: (o) experimental and (—) calculated intensities. The difference between both intensities is shown at the bottom of the figures (—).The Bragg reflections is shown for Fe3C (|), α-Fe (|) and graphitic carbon (|).

Table II: Weight percent (*wt %*) and lattice parameters of the crystalline phases estimated through the Rietveld refinement of the X-ray diffraction patterns. The error in the lattice parameters appears in the last digit.

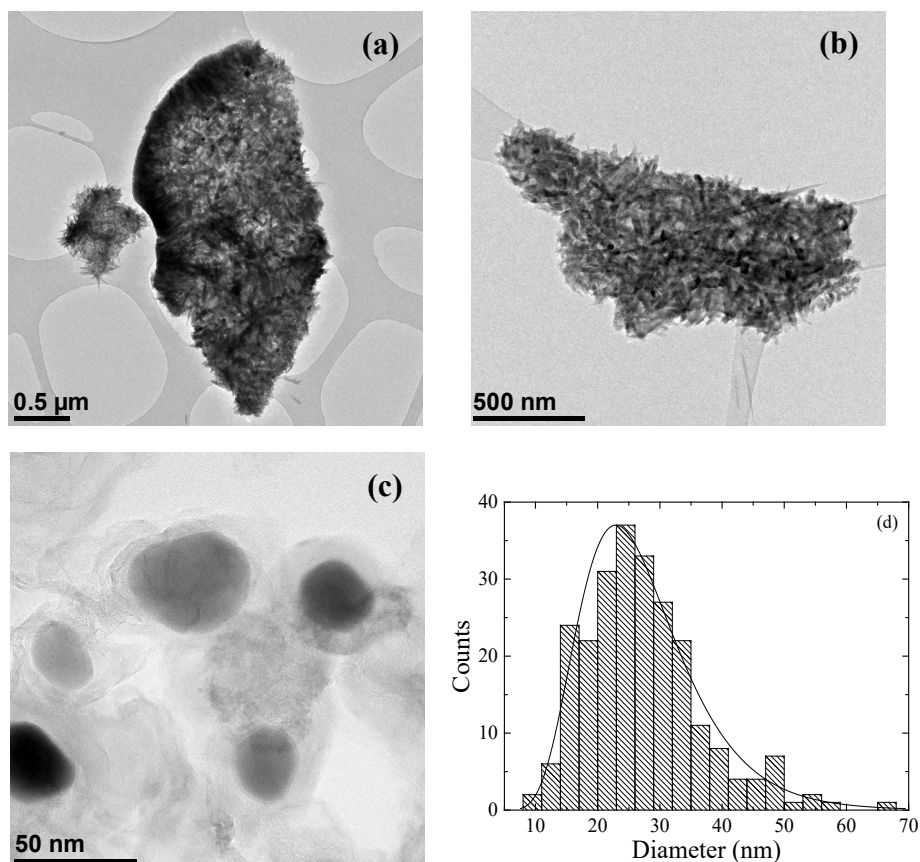| Sample	*Fe₃C* wt %	a (Å)	b (Å)	c (Å)	d (nm)	*α-Fe* wt %	a (Å)	d (nm)	*Carbon-based* wt %	a (Å)	c (Å)	d (nm)	*Fe₃O₄* wt %	a (Å)	d (nm)
A-Fructose800	12	5.092	6.742	4.527	16.0	2	2.8662	126.9	86	2.487	6.846	3.4			
A-Glucose800	12	5.078	6.733	4.519	31.3	5	2.8622	57.7	83	2.475	6.84	2.2			
A-Sucrose600	22	5.087	6.741	4.523	38.3	2	2.8663	100.3	76	2.49	6.96	0.9			
A-Sucrose800	12	5.091	6.744	4.527	41.1	0	2.8691	126.9	86	2.4591	6.811	5.4	2	8.479	14.4

Fig. 4: TEM images for A-fructose (a) 400, (b) 600 and (c) 800. (d) Nanoparticle grain distribution (histogram) for A-fructose800.

Transmission Electron Microscopy (TEM) was employed to further analyze the crystalline phase distribution in the A-*sugar* samples. Firstly, fig. 4 shows the images of the annealed samples synthesized employing fructose (a) T_{ann} = 400, (b) 600 and (c) 800 ^{0}C. The images confirm the previous X-ray diffraction analysis: well defined Fe-based spherical nanoparticles surrounded by a graphitic shell for T_{ann} = 800°C, and a distribution not so well defined for lower annealing temperatures. In those initial reduced states (low T_{ann}), elongated particles are clearly visible, particularly for the sample annealed at 600°C. This elongated shape is a common feature of Fe hydroxides widely reported in the literature [90, 91]. Fig. 4e shows the nanoparticle size distribution for T_{ann} = 800°C, where a lognormal distribution

is obtained with mean grain sizes $\langle d \rangle = 26 \pm 1$ nm. The lower mean grain size obtained from the X-ray diffraction (16 nm) could indicate a polycrystalline nature of the precipitated grains. Nevertheless, a small fraction of larger grains can also be detected (tail in the nanoparticle size histogram) that would probably correspond to the α-Fe phase detected by X-ray diffractometry and would also contribute to the higher mean grain size estimated through the nanoparticle histogram.
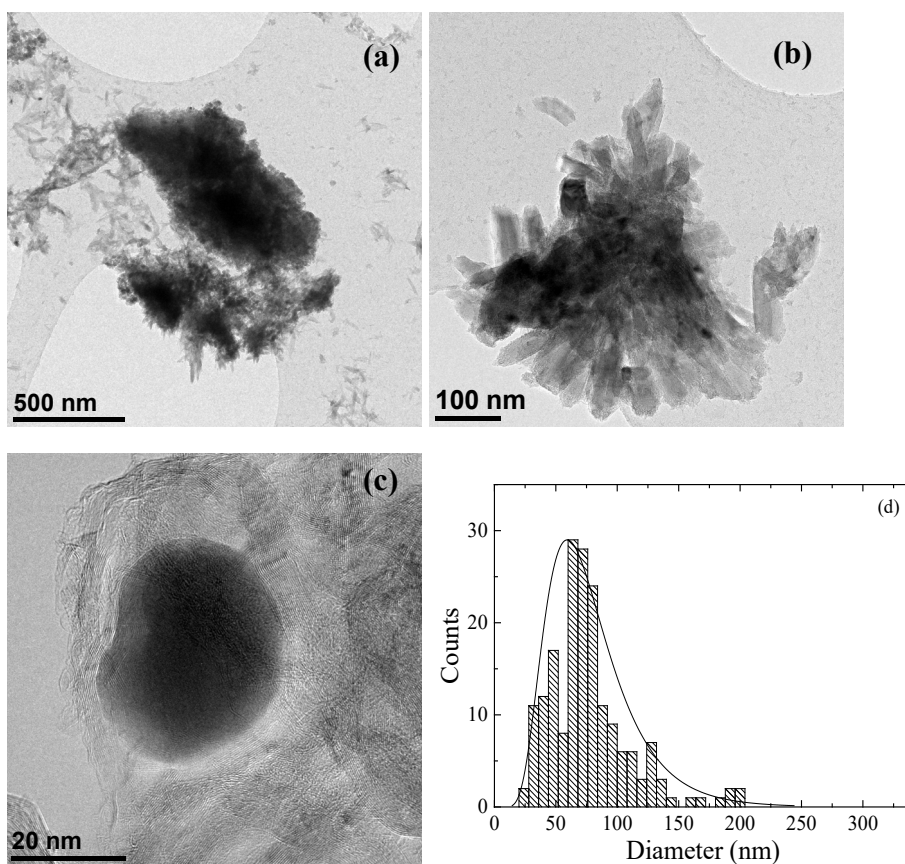

Fig. 5: TEM images for A-glucose (a) 400, (b) 600 and (c) 800. (d) Nanoparticle grain distribution (histogram) for A-glucose800.

Similarly, fig. 5 shows the images for the nanoparticles obtained employing glucose as reducing agent. Again, high temperature annealings are needed (T_{ann} = 800°C, see fig. 5c) to obtain Fe-based nanoparticles surrounded by a graphitic shell. As fig. 5d shows, a lognormal distribution also describes the nanoparticle distribution diameters, but with a slight increase in the mean grain diameter ($<d>$ = 73 ± 2 nm). In this case, the occurrence of larger grains (hundreds of nanometers in size) are again clearly visible in the histogram`s tail (see fig. 5d). Furthermore, as in case of the previous fructose sample, for lower annealing temperatures, similar elongated structures can be visualized, with well-defined elongated nanoparticles for the intermediate annealed state (T_{ann} = 600°C, see fig. 5b).
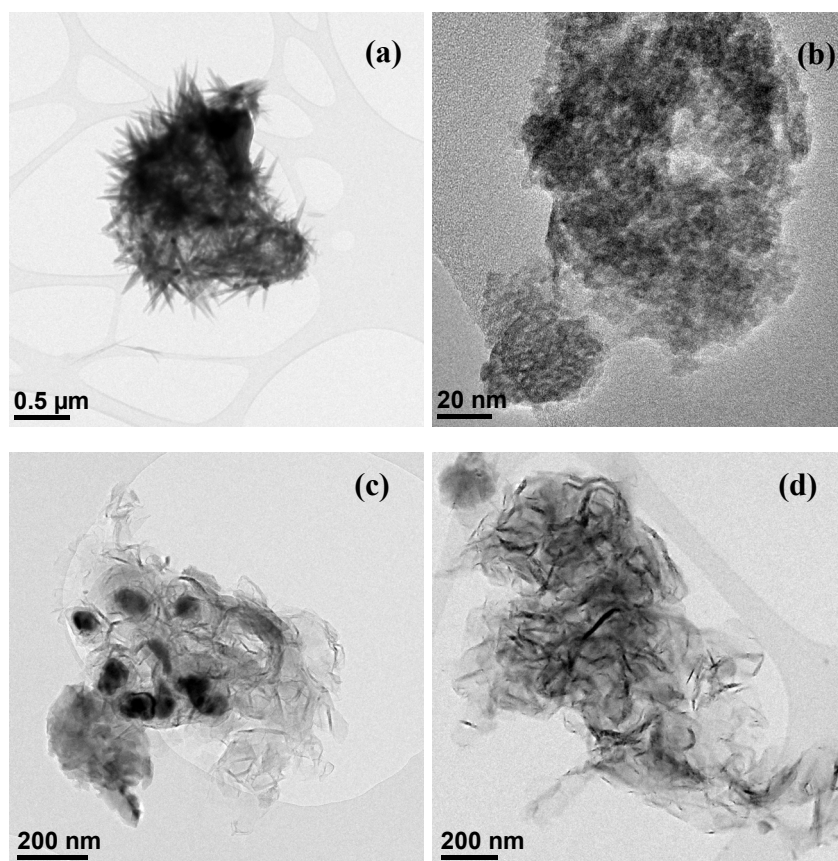

Fig. 6: TEM images for A-sucrose (a) 400, (b) and (c) 600 and (d) 800.

Finally, the images of the sample synthesized with sucrose are depicted in fig. 6. In this sample, a clear distribution of elongated nanoparticles is seen for T_{ann} = 400°C. On the contrary, the images for T_{ann} = 600^{0}C show the coexistence of an ultrafine structure (nanoparticles around 4 nm) and larger Fe-based nanoparticles with mean grain sizes around 90 nm (fig. 6b and c). However, the images of the A-sucrose800 sample show mostly ordered carbon (graphene flakes) being only visible few number of Fe-based nanoparticles embedded in the carbon matrix. The large amount of graphitic carbon could hinder a clear visualization and prevents the estimation of a proper nanoparticle size distribution.

Raman spectroscopy is a powerful research tool to investigate carbon based materials. In fact, Raman signals arising from lattice vibrations (phonons) in graphitic materials are very sensitive to the degree of structural disorder [92]. Accordingly, in order to analyze the evolution (order state) of the carbonaceous matrix in the annealed state, the Raman spectra were analyzed in A-*sugars* samples, annealed at 600 and 800°C. Fig. 7 shows the obtained Raman spectra employing fructose as a reducing agent. In order to properly analyze the samples, at least 30 different zones per sample were analyzed to gain insight into the structure of the material. The spectra are different depending on the zones, but all of them can be classified in two types. In general, there is a predominant type of spectra for each sample. So, the spectra can be classified belonging to Majority (*M*) or minority (*m*) zones, employing as an additional tool a color CCD sample viewing system with image capture capability.
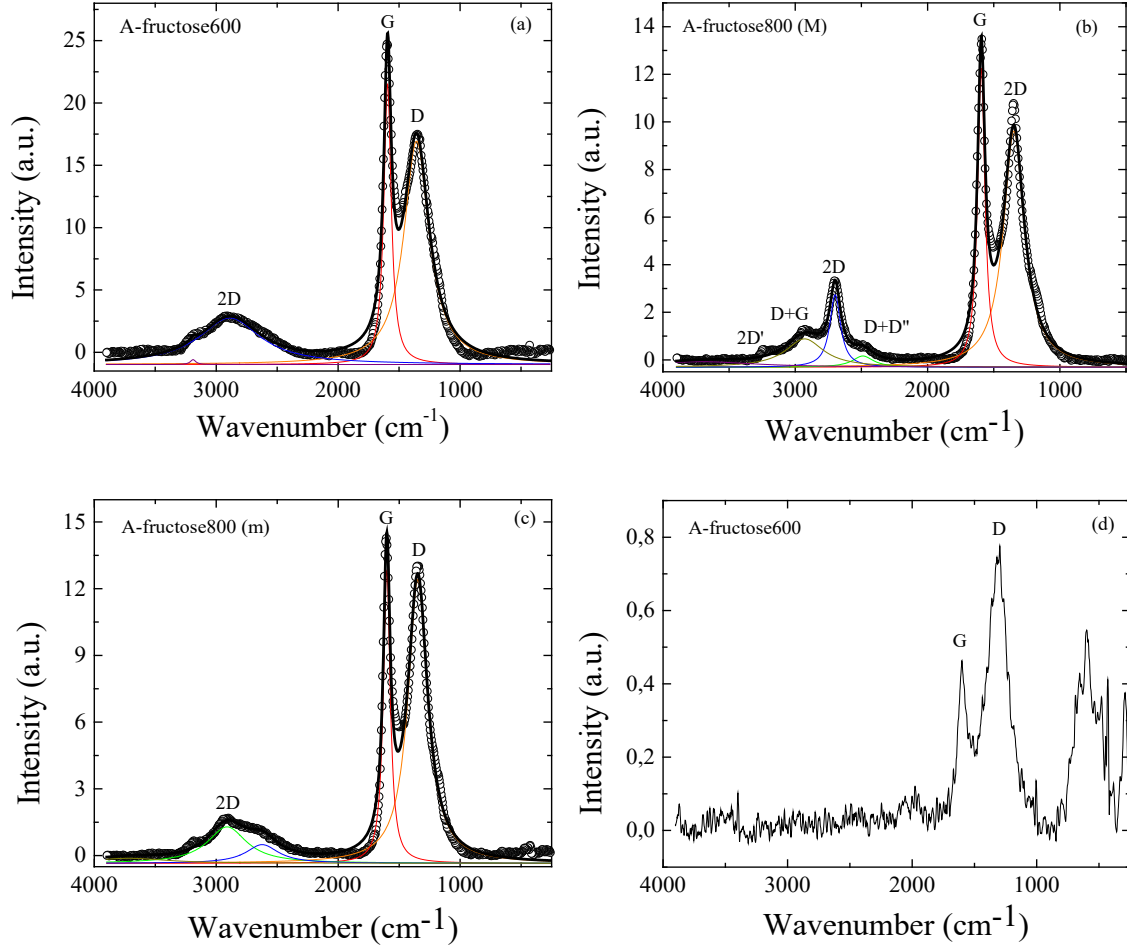
Fig. 7: Raman spectra for the annealed samples employing fructose as reducing agent: (a) $T_{ann} = 600°C$; $T_{ann} = 800°C$ (b) majority (M) and (c) minority (m) areas; (d) Raman spectra of a selected area containing oxides (A-fructose600): (o) experimental and (—) sum of the deconvoluted peaks.

The spectra can be characterized in the first order region (1100-1800 cm^{-1}) by the G and the D bands around $\omega_G \approx 1590$ cm^{-1} and $\omega_D \approx 1350$ cm^{-1}, respectively. The G band, primary mode in graphene and perfect crystalline graphite, is an in-plane vibrational mode involving the sp^2 hybridized carbon atoms (stretching vibration). However, the D band, known as the disordered band or defect band, represents a breathing mode from the sp^2 carbon rings that to be active should be adjacent to a layer edge or defect. Furthermore, in the second order region (2200-3400 cm^{-1}), the second order of the D band (2D, overtone of

the D band also denominated as G' band) at $\omega_{2D} \approx 2890$ cm^{-1} is mainly detected, and its activation does not require defects and is always present in crystalline carbon materials [93].

Table III: Raman parameters for the selected annealed samples.

sample	Region	ω_D (cm^{-1})	ω_G (cm^{-1})	$FWHM_D$ (cm^{-1})	$FWHM_G$ (cm^{-1})	I_D/I_G	ω_{2D} (cm^{-1})	I_{2D}/I_D
A-fructose600	M	1356.4±0.5	1594.7±0.5	251.2±1.7	72.8±0.6	0.79	2889±3	0.21
A-fructose800	M	1347.7±0.3	1594.2±0.5	192.3±1.0	67.2±0.6	0.79	2698.4±0.7	0.31
	m	1347.2±0.3	1601.7±0.5	195.2±1.0	68.2±0.5	0.97	2911±7	0.13
A-glucose600	M	1358.4±0.5	1595.6±0.2	252.5±1.7	75.1±0.6	0.81	2888±3	0.22
A-glucose800	M	1353.3±0.4	1600.8±0.2	233.0±1.4	73.4±0.6	0.88	2863±3	0.19
	m	1355.76±0.08	1594.31±0.06	53.1±0.2	44.44±0.17	0.78	2702.0±0.1	0.78
A-sucrose600	M	1339.8±0.4	1591.7±0.2	228.8±1.4	72.7±0.6	0.82	2846±3	0.18
	m	1346.42±0.08	1581.67±0.07	53.1±0.3	41.77±0.19	0.81	2691.1±0.1	0.58
A-sucrose800	M	1356.3±0.1	1594.46±0.05	65.0±0.3	44.05±0.15	0.58	2704.6±0.1	1.02
	m	1356.7±0.3	1598.4±0.2	219.5±1.2	78.4±0.7	1.02	2869±4	0.14

In the case of A-fructose600 no distinction between *M* and *m* areas can be visualized, but a single characteristic spectrum shown in fig. 7a. However, for the fructose sample annealed at 800°C, two different Raman spectra are found for T_{ann} = 800°C ascribed to majority (*M*) and minority areas (*m*), fig. 7b and 7c, respectively. It should be noted that this A-fructose800 sample shows additional peaks in the second order region that can be properly deconvoluted employing Lorentz peak bands: $\omega_2 \approx 2450$ cm^{-1}, $\omega_3 \approx 2950$ cm^{-1}, and $\omega_4 \approx 3200$ cm^{-1} (the solid black line of the Raman spectra represents the sum of the deconvoluted peaks). In fact, similar overtones have been reported in graphitic based nanostructures [94, 95], and usually denominated as *D+D''*, *D+G* and *2D'*, respectively. Furthermore, the occurrence of

a small fraction of Fe oxides (Fe_3O_4) can be also detected in the samples, whose characteristic Raman spectra is shown in fig. 7d ($\omega_{Fe3O4} \approx 650$ cm^{-1}) [96].

Table III reports the fitted Raman parameters for the set of the analyzed samples employing the Lorentz peak deconvolution: the mean Raman peaks (ω_D, ω_G and ω_{2D}), including the full width at half maximum (FWHM) for both D and G bands and the relative peak intensities of the first and second order regions (I_D/I_G and I_{2D}/I_D). Firstly, focusing on the fructose sample, both annealed states (600 and 800°C, M and m areas) display similar ω_D and ω_G Raman shift values. For $T_{ann} = 800$°C, a slight decrease in FWHM is detected for D and G Raman peaks in both M and m areas. In fact, the linewidth has been extensively used in the characterization of the crystalline size (L_a, structural correlation length) of the graphitic phase (FWHM $\propto$ 1/ L_a) [97]. Thus, the detected decrease in FWHM would confirm the increase in the carbon ordering upon annealing as the TEM images reflects (see fig. 4, where graphitic ordered layers can be visualized for $T_{ann} = 800$°C surrounding Fe nanoparticles).

On the other hand, the relative intensities I_D/I_G and I_{2D}/I_D can be employed to follow the disorder state. As previously indicated, the D band is usually known as the disordered band and the ratio I_D/I_G is employed to characterize the state of the disorder in the carbon based materials, monitoring the amount of defects or the extent of deviation of the crystalline arrangement from perfect hexagonally organized planar C network [98]. However, the second order $2D(G')$ is reinforced by long-range graphitic order and the intensity ratio I_{2D}/I_D is considered as a long-range order indicator, being quite sensitive to the overall crystalline quality of the graphitic network. Thus, a decrease in I_D/I_G and an increase in I_{2D}/I_D would be indicative of a reinforcement in the state of local and long-range order of the carbonaceous

matrix. Thus, focusing on the A-fructose800 sample, the minority area spectra (m) display the highest and lowest I_D/I_G and I_{2D}/I_D ratios, respectively, indicating the highly disorder of this residual minority carbon phase.
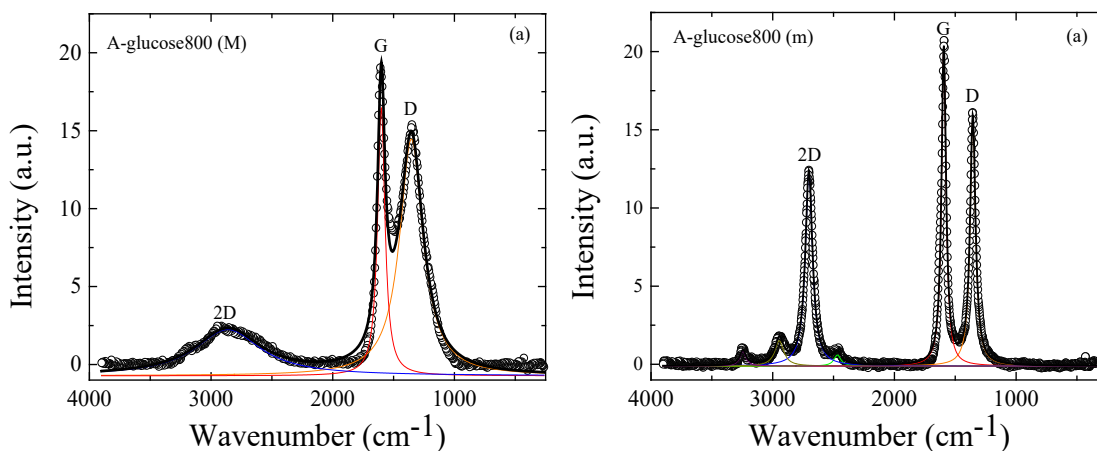

Fig. 8: Raman spectra for the A-glucose800 sample: (a) majority (M) and (b) minority (m) areas: (o) experimental and (—) sum of the deconvoluted peaks.
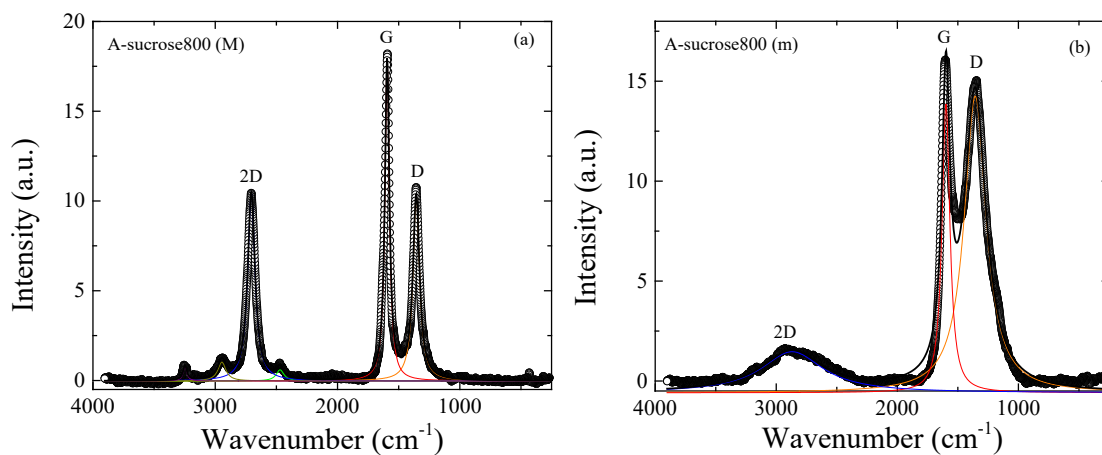

Fig. 9: Raman spectra for the A-sucrose800 sample: (a) majority (M) and (c) minority (m) areas: (o) experimental and (—) sum of the deconvoluted peaks.

Regarding the sample reduced with glucose, a similar evolution in the Raman spectra is found with the annealings. A disordered carbon state at $T_{ann} = 600°C$ (Raman spectra

similar to that displayed in fig. 7a) and 2 different regions (M and m) for the higher temperature annealing T_{ann} = 800°C. However, as fig. 8 shows certain differences can be found in A-glucose800 when comparing with the A-fructose800 sample, namely a wider 2D band for the M region and a more defined second order peaks for the m spectra (fig. 8a and 8b, respectively). In fact, a highly disorder majority state is found in this annealed state when compared to the sample reduced with fructose for T_{ann} = 800°C. The most remarkable features of the highly ordered minority (m) A-glucose800 spectrum are a reduction in both FWHM$_D$ and FWHM$_G$ band widths, together with the relative decrease and increase in I_D/I_G and I_{2D}/I_D, respectively.

Finally, when sucrose is employed as reducing agent, two differentiated regions (M and m) are detected in both annealed samples (600 and 800°C). Fig. 9 shows the obtained spectra for T_{ann} = 800°C, where the majority (M) region is characterized by narrow G and D peaks and multiple peaks in second order zone and the minority (m) region displays similar spectra as the previously carbon disordered regions (see for instance, fig. 7a). However, an opposite behavior is found for the sample annealed at 600°C, namely, disordered spectra for the majority (M) area and narrow Raman peaks in the minority (m) regions. This evolution is clearly reflected in the fitting parameters displayed in table III: (i) low FWHM (D and G) values for A-sucrose600 (m) and A-sucrose800 (M) (and vice versa); (ii) minimum and maximum I_D/I_G and I_{2D}/I_D values, respectively, in the highly ordered A-sucrose800 (M) sample.

Finally, jointly analyzing the Raman parameters obtained (i.e. Raman shifts) for the set of the analyzed samples, while negligible variations are found in ω_D and ω_G, a relationship between the carbon order state and ω_{2D} can be inferred. As table III shows, those

spectra characterized by a higher degree of order (i.e. reduced I_D/I_G) displays $\omega_{2D} \approx 2700$ cm^{-1}, while a shift towards higher wavelength ($\omega_{2D} \approx 2850$- 2910cm^{-1}) is found in the spectra of those samples or regions with a higher disordered state.

As final conclusion from the Raman spectroscopy analysis it can be outlined the increase in the order degree of the carbonaceous matrix with the annealing temperature. Particularly, similar ordering process is deduced for the fructose and glucose samples: for T_{ann} = 600°C a majority disordered phase; at T_{ann} = 800°C a partial ordering in the major areas of the carbon matrix, coexisting with minor ordered zones. However, a slightly higher degree of order is detected in the minority areas of the A-glucose800 sample. However, the sucrose sample displays at T_{ann} = 600°C similar Raman spectra than the other samples reduced at higher temperature (T_{ann} = 800), again confirming previous structural characterizations. The reduction with sucrose at high temperature (A-sucrose800) gives rise to a well ordered carbon phase as main contribution, where a residual minority disordered contribution can also be detected.

3.3. Magnetic characterization
3.3. a. dc magnetic characterization

Firstly, regarding the magnetic characterization of the samples, fig. 10a-c shows the temperature dependence of the high field magnetization, M, (applied field μ_0H = 6T) for the A-glucose, A-fructose and A-sucrose samples (a, b and c, respectively) at different annealing temperatures.
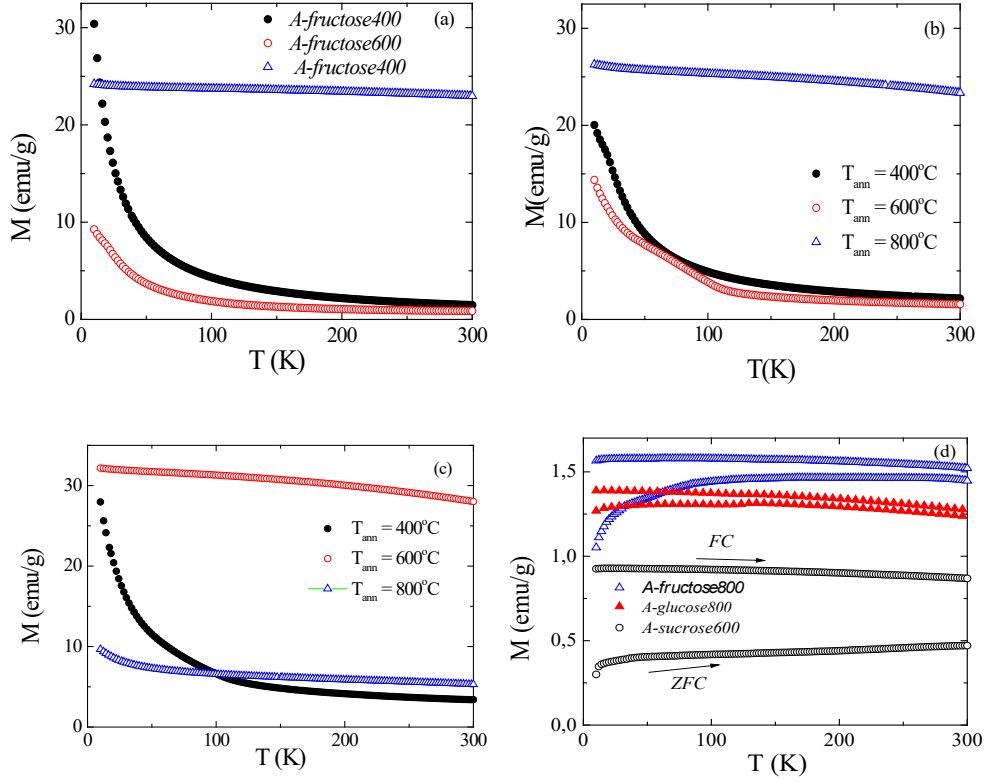
Fig. 10: High field magnetization (applied field $\mu_0 H = 6$ T) versus temperature (T) for (a) fructose, (b) glucose and (c) sucrose; (d) *ZFC-FC* magnetization curves for the selected high saturation magnetization samples (applied field $H = 50$ Oe).

The annealed samples display at low annealing temperature ($T_{ann} = 400°$C), for fructose and glucose, a sharp magnetization decrease that could be indicative of antiferromagnetic response. In fact, $M(T)$ curves can be fitted in the low temperature region to the Curie-Weiss law ($M = \frac{C}{T-\theta} H$; with C the Curie constant and θ the characteristic critical temperature). Table IV summarizes the obtained fitting parameters for both samples ($C_H = CH$). The negative value of the critical temperature, θ, confirms the antiferromagnetic nature of the samples. It should be noted that the fitting procedure cannot be properly done in the A-sucrose400 sample. As fig. 10c shows, at least an additional magnetic contribution is clearly visible for 45 K $\leq T \leq$ 125 K. Similar effect can be detected for A-glucose600 and in a lesser

27

extent in A-fructose600 (see fig. 10b and a, respectively). As previously discussed, the precipitation of Fe-based nanoparticles is already detected for A-sucrose600 sample and can be directly confirmed though the *M-T* curves. As in the case of A-fructose800 and A-glucose800, the temperature dependence of *M* displays in this sample the typical Bloch`s law ascribed to the spin wave excitations in ferromagnetic materials: $M = M_0(1 - BT^n)$, with M_0 the spontaneous magnetization at 0 K, *B* the Bloch constant and *n* a parameter which value depends on the size of the particles. Moreover, in order to properly fit the magnetization curves in these reduced samples, and additional Curie-Weiss contribution should be also included [56]:

$$M = M_0(1 - BT^n) + \frac{C_H}{T - \theta} \qquad (2)$$

Table IV summarizes the fitting parameters obtained in these ferromagnetic samples. Regarding the Bloch constant, the values are close to the reported values for bulk coarse-grained Fe ($B \approx 3 \ 10^{-6} \ K^{-3/2}$) [99]. However, a higher value of B ($\approx 3 \ 10^{-5} \ K^{-3/2}$) is reported in Fe-C nanostructures [56, 100]. Notice that in the present case the estimated temperature exponent, *n*, is higher than the exponent for bulk systems (*n* = 3/2). In fact, values close to 2 have been extensively reported in nanoparticles systems due to size effects [101]. Nevertheless, when *n* > 3/2 is considered, a similar reduction in the Bloch ($B \approx 1 \ 10^{-7} \ K^{-5/2}$) is found in carbon encapsulated Fe_3C nanostructures [102].

Table IV: Magnetic parameters obtained from the fitting of *M(T)* to the Bloch's law (eq. 2). Saturation magnetization, M_S, obtained from the estimated magnetic phase distribution (table II).

sample	M_S (emu/g)	M_0 (emu/g)	B (10^{-6})	n	C_H (emu/g K)	θ (K)
A-fructose400	--	--	--	--	462±1	-4.80±0.06
A-fructose800	21.2	23.75±0.01	0.68±0.07	1.89±0.02	9.1±0.4	-9.9±0.8
A-glucose400		--	--	--	539±3	-10.8±0.2
A-glucose800	27.8	25.34±0.01	1.5.±0.2	1.90±0.02	28±1	-19.9±0.8
A-sucrose600	35.2	31.66±0.02	3.7±0.3	1.80±0.02	14±1	-17±2
A-sucrose800	18.6	5. 76±0.01	2.4±0.5	1.91±0.03	104±1	-16.5±0.2

With respect to the saturation magnetization, M_0, the obtained values mainly reflects the magnetic phase distribution found in the X-ray diffraction patterns (see table II). Table IV includes the estimated values for the saturation magnetization, M_S, assuming this magnetic phase distribution and M_S bulk for Fe_3C and α-Fe ($M_s(Fe_3C) = 140$ emu/g; $M_s(\alpha\text{-Fe}) = 220$ emu/g): $M_s = x_{Fe_3C}M_S(Fe_3C) + x_{\alpha-Fe}M_S(\alpha - Fe)$, for *A-sucrose800*, the M_S contribution (2%) of Fe_3O_4 (92 emu/g) is also included. Note that in most of the samples a lower M_0 value is obtained in comparison with the estimated M_S magnetization. Such differences could be ascribed to the existence of spin disordered effects inherent in nanoparticle systems, leading to a decrease in the nanoparticle saturation magnetization with respect to the bulk [51, 103]. However, in particular the sample reduced with sucrose at 800°C displays (see also fig. 10c) a remarkable decrease in magnetization. Such a decrease cannot be explained in terms of a partial oxidation since only a small amount of Fe_3O_4 can be detected in the X-ray pattern. Indeed, reduced magnetization values have been also reported in other Fe-C nanostructures [100], but no clear explanation is provided but a correlation with the enhancement in the surface spin disordered effects. In the present case, the decrease in magnetization is

accompanied by an increase in the antiferromagnetic contribution (increase in C_H, see table IV) that could support this assumption. However, it should be notice that this effect is associated with an enhancement of the order degree of the carbon matrix (see Raman analysis), also reported in a previous study [104]. Thus, the magnetic surface disordered effects as a result of the interaction with the carbon matrix could be also coupled with the formation of antiferromagnetic phases (i.e. γ-Fe) on the particle surface hardly detectable by X-ray diffractometry. In fact, the occurrence of antiferromagnetic γ-Fe is characteristic feature of Fe-C nanostructures [105], particularly in the growth of highly ordered carbon nanotubes [106, 107].

Nevertheless, the diamagnetic nature of the graphite has not been taken into account in the previous characterization. Assuming a magnetic susceptibility of -10^{-6} emu/gOe [108], a diamagnetic contribution around -0.1 emu/g at 6 T would not significantly modify the results displayed in table IV. Regarding the low field magnetization process, these ferromagnetic samples displays soft magnetic behavior characterized by reduced remanence magnetization, $M_r/M_S \leq 0.05$, and low coercive field, $Hc \leq 100$ Oe (8 A/m), in the limit of the SQUID magnetomer sensitivity. Superparamagnetic behavior can be excluded taking into account the large mean particle diameter of the samples in comparison with the reported superparamagnetic Fe_3C or α-Fe mean sizes (units of nm) [109, 110]. Moreover, the *ZFC-FC* magnetization curves do not indicate the occurrence of superparamagnetism at room temperature (see fig. 10d), i.e. maximum in the *ZFC* magnetization at the blocking temperature and splitting of the *ZFC-FC* curves for lower measuring temperatures. Therefore, the nearly anhysteretic *M-H* curves should be ascribed to the soft magnetic

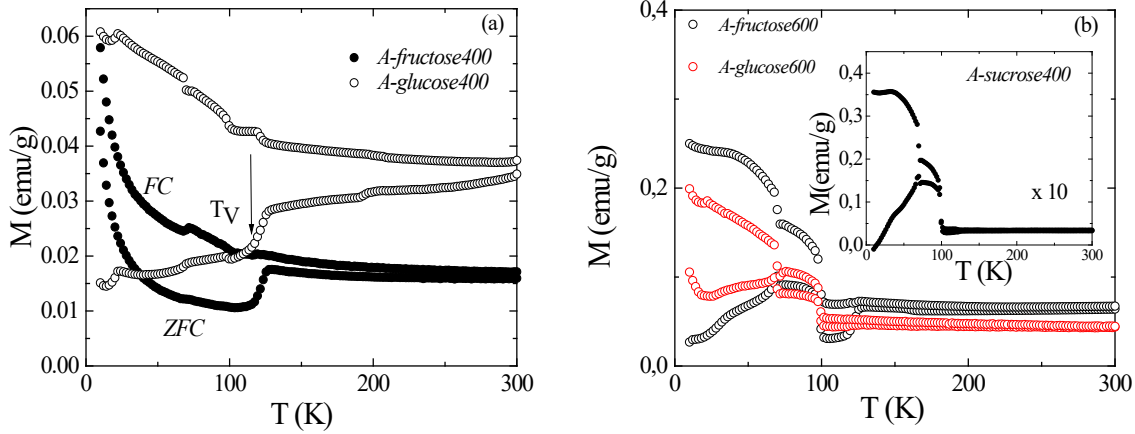behavior of the samples as a consequence of the large mean grain sizes of the Fe_3C and α-Fe nanoparticles.

Fig. 11: *ZFC-FC* magnetization curves for the samples reduced with fructose and glucose at (a) T_{ann} = 400°C and (b) T_{ann} = 600°C (inset in (b): *ZFC-FC* for A-sucrose400 (applied field H = 50 Oe).

Furthermore, *ZFC-FC* curves could also provide insight about the initial stages of the decomposition process. Fig. 11 shows the *ZFC-FC* curves for the samples reduced with fructose and glucose at (a) T_{ann} = 400°C and (b) T_{ann} = 600°C. The occurrence of small fraction of magnetite (Fe_3O_4) can be deduced at the initial stages of decomposition (T_{ann} = 400°C, fig. 11a) for the fructose and glucose samples, from the kink in the *ZFC* magnetization at the characteristic Verwey temperature ($T_V \approx$ 120 K) [111]. However, the low field magnetization for the sucrose sample shows at T_{ann} = 400°C (see inset of fig. 11b) a different temperature evolution. A complex magnetic transition for $T \leq$ 100 K is found, similar to that displayed by the annealed samples with fructose and glucose at T_{ann} = 600°C. These results confirm once more, the initiation of the decomposition process at lower annealing temperatures when sucrose is employed as reducing agent.

3.3. b. ac magnetic characterization. SAR estimation

The *ac* hysteresis loops were obtained at two exciting frequencies, f = 45 and 477 kHz. Due to the experimental limitations, the amplitude of the *ac* magnetic field, H_{ac}, was limited to 58 kA/m and 30 kA/m for the low and high f, respectively. Fig. 12 shows the estimated *SAR* values through the area of the *ac* hysteresis loop (eq. 1), for A-fructose800, A-glucose800 and A-sucrose600 samples (a, b, and c, respectively) as a function of the amplitude of applied magnetic field, H_{ac}. The inset of the figures also shows the evolution *ac* coercive field, H_C, at both frequencies. These samples were chosen due to the maximum magnetization ascribed to the occurrence of ferromagnetic Fe_3C nanoparticles (see Fig. 10). As expected, maximum *SAR* values are obtained for f = 477 kHz due to the increase in the magnetic losses with frequency. In order to comparatively analyse the heating efficiency of the three samples, table V summarizes the maximum *SAR* values achieved at both frequencies.
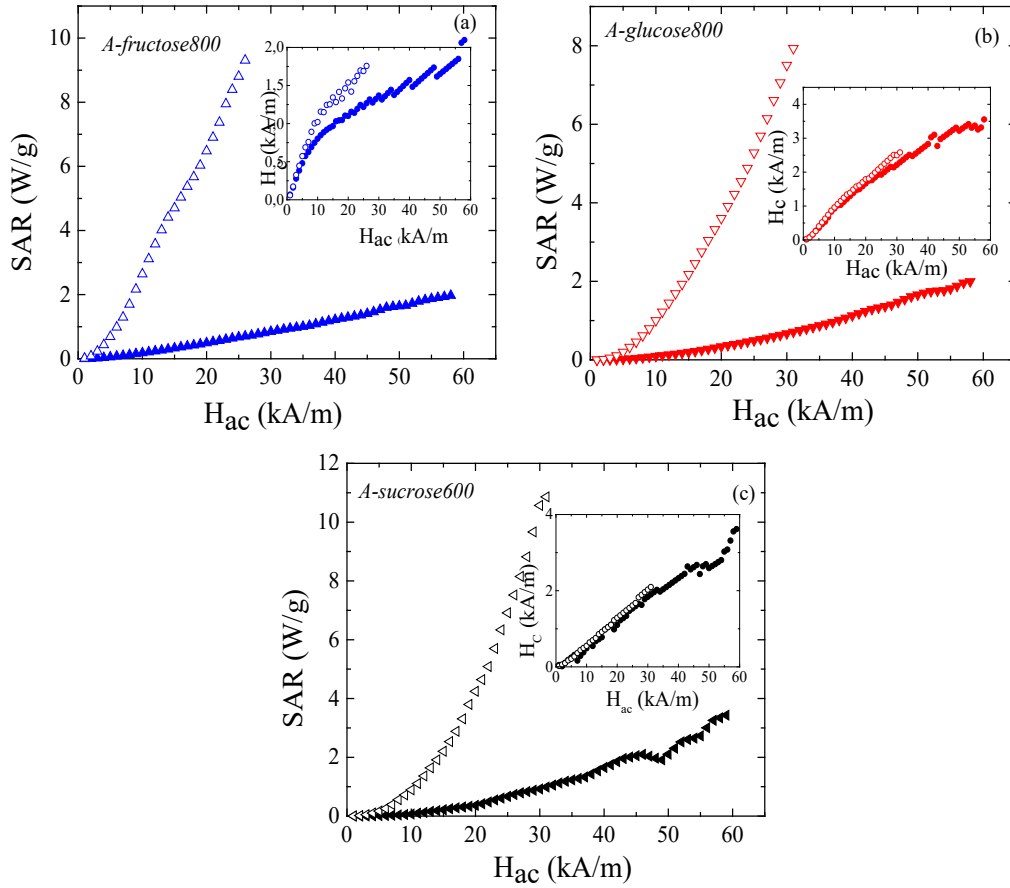
Fig. 12: *SAR* as a function of the amplitude of the *ac* magnetic field, H_{ac}, for f = 45 kHz (open symbols) and 477 kHz (close symbols) for (a) A-fructose800, (b) A-glucose800 and (c) A-sucrose600. The inset of the figure shows the evolution of the coercive field, H_C, under the same experimental conditions.

The samples would display moderate heating efficiency, comparing the estimated *SAR* with the typical values reported in the literature for Fe oxides nanoparticles ($\approx$ 1 kW/g) under similar experimental conditions [112]. Even taking into account the normalization employing *%wt* of the magnetic nanoparticles (g_{Fe}) (Table II), *SAR* remains one order of magnitude below the optimum reported values for magnetite and maghemite nanoparticles.

Table V: Maximum estimated *SAR* values for both frequencies in W/g. The values at f = 477 kHz are normalized to the *%wt* (g_{Fe}) estimated through the estimated magnetic phase distribution (table II).

sample	SAR (W/g) f = 45 kHz, H_{ac} = 58 kA/m	SAR (W/g) f = 477 kHz H_{ac} = 26 kA/m	SAR (W/g_{Fe}) f = 477 kHz H_{ac} = 26 kA/m
A-fructose800	1.97	9.31	70.5
A-glucose800	1.99	5.70	32.4
A-sucrose600	3.42	7.51	31.3

Two strategies can be employed to optimize *SAR* (increase the area of the hysteresis loops): increase of the saturation magnetization, M_S, and enhancement of the magnetic (mainly magnetocrystalline) anisotropy, K. Furthermore, the magnetization process, and thus the area of the hysteresis loops, depends not only on these intrinsic magnetic parameters, but also on the nanoparticle size distribution and effective magnetic interactions between the nanoparticles [113, 114]. Thus, maximum *SAR* values are reported for magnetic nanoparticles sizes around the monodomain-multidomain critical size, D_{SD}, and under particle chain arrangements that enhance the effective magnetic anisotropy [115].

In the present nanocomposites, both ferromagnetic Fe_3C and α-Fe fulfil the magnetization increase in comparison with the ferromagnetic Fe_3O_4 and γ-Fe_2O_3 nanoparticles. Beside this, they display a slight enhancement of the magnetic (magnetocrystalline) anisotropy ($K_{Fe} \approx 5\ 10^4$ J/m^3 [116]; $K_{Fe3C} \approx 10\ 10^4$ J/m^3 [117], bulk at room temperature) in comparison with the magnetocrystalline anisotropy for bulk magnetite ($K_{Fe3O4} \approx 1\ 10^4$ J/m^3 [51]). In fact, *SAR* values around 3 kW/g are reported in water dispersed Fe^0 (α-Fe) nanoparticles ($\approx$ 10 nm) [114], but with reduced chemical stability (i.e. sharp reduction of the saturation magnetization with air exposure) that limits their potential

application [118]. Regarding Fe_3C nanoparticles, few reports are available in the literature analyzing their magnetic hyperthermia or induction heating response. While $SAR \geq 1$ kW/g are found in some colloidal Fe carbide nanoparticles with grain sizes below 25 nm [114, 118, 119], other works display moderate SAR values like those displayed in table V [58].

Regarding the effect of the nanoparticle size (see fig. 13), for the multi-domain regime ($d > D_{SD}$), the ac coercive field (H_C) is lower due to the formation of magnetic domains [120] and hence, the ac hysteresis area and SAR are reduced. For slightly elongated metallic iron particles, D_{SD} is estimated to be around 20 nm [121]. Therefore, the α-Fe nanoparticles on this work with crystal sizes larger than 60 nm (Table II) completely fall into multi-domain regime and hence, they scarcely contribute to the SAR values. In fact, a sharp reduction in SAR is reported on literature for large Fe nanoparticles (> 20 nm) due to the multidomain state [114].

The Fe_3C nanoparticles with mean crystal sizes ranging from 16 to 40 nm (see table II), exhibit both single and multi-domain features. The magnetization loops for A-fructose800 and A-glucose800 i.e. is the sum of a typical single-domain (Fe_3C nanoparticles) and a multiple-domain (Fe_3C/α-Fe nanoparticles) cycle. However, the ac cycle of sample A-sucrose should be correlated only to multi-domain behavior, in good agreement with their larger crystal sizes of Fe_3C particles (see table II, d(A-sucrose600) = 38 nm).
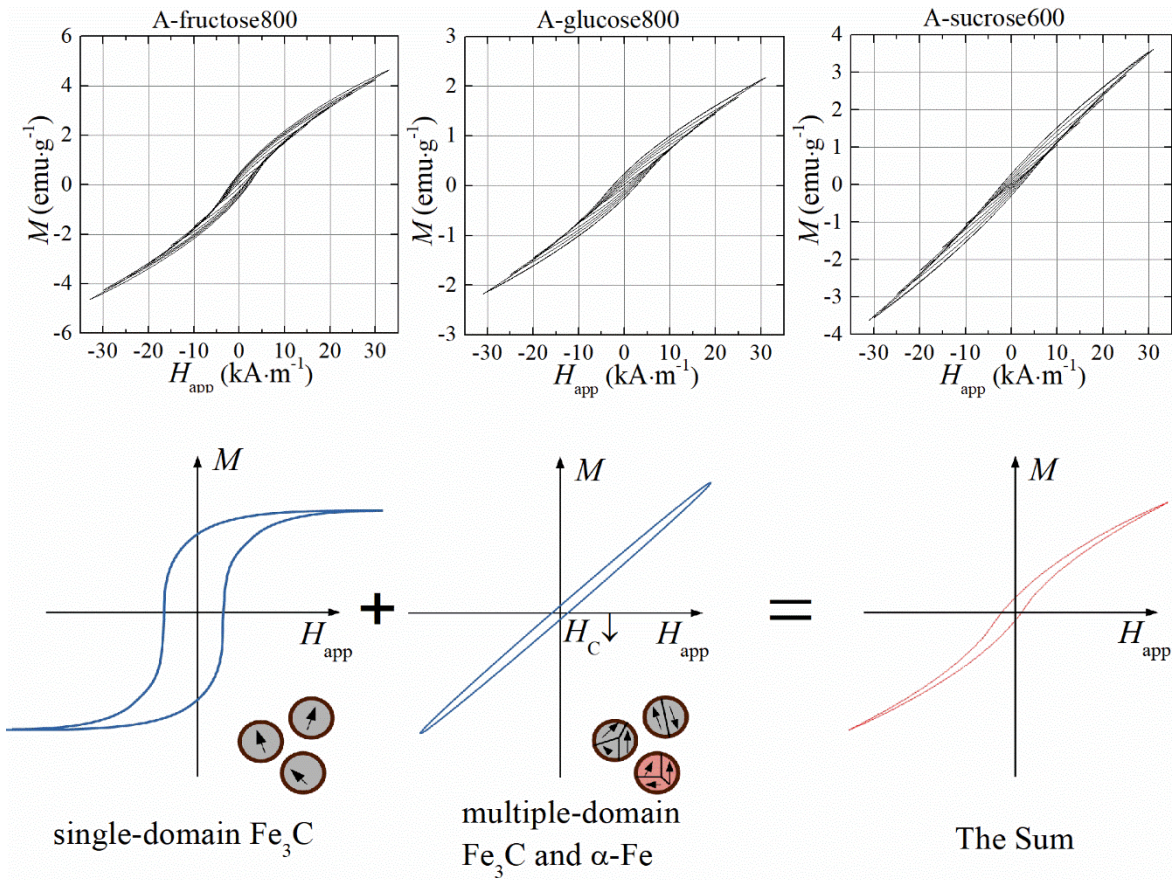
Fig. 13: *ac* hysteresis loops at 477 kHz. Below, schematic cycles of large single-domain and larger multi-domain nanoparticles are plotted. For samples A-fructose800 and A-glucose800, the measured cycle is the composition of single-domain and multi-domain cycles whereas for sample A-sucrose600, only multi-domain particles contribute.

Thus, it should be noted a correlation of the maximum estimated *SAR* values in the samples and the mean grain sizes for the Fe_3C nanoparticles (see table II, *d*(A-fructose800) = 16 nm; *d*(A-glucose800) = 31 nm; *d*(A-sucrose600) = 38 nm). Namely, the highest *SAR* value in the A-fructose800 sample corresponds with the smaller mean grain size. For 16 nm diameter iron carbide nanoparticles, most of the iron grains are single-domain and hence, they present higher *SAR* values. In addition, it can be appreciated an increment of the coercivity field with frequency (inset on figure 12a), indicating the presence of some amount

36

of magnetic nanoparticles in the superparamagnetic regime (i.e. thermal fluctuation driven dynamic magnetization). To sum up, the multiple domain formation on iron carbide and α-Fe MNPs significantly reduces the measured SAR values. In addition, dipolar interactions between the magnetic nanoparticles inside the carbon matrix may reduce the heating ability of the analyzed samples [122].
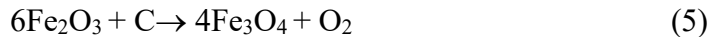
It should be finally pointed out that typical experimental values for hyperthermia applications in medical treatments are $f = 100$ kHz and $H_{ac} = 20$ kA/m ($H_{ac}f \leq 5 \times 10^9$ A m^{-1} should be fullfiled [123]). Nevertheless, as previously described, these Fe based carbonaceous nanocomposites are currently and extensively analyzed for environmental applications, such as nanoadsorbents and nanocatalysts. The local increase in temperature has been reported to improve the adsorbing and chemical reactivity properties of these carbonaceous nanocomposites. Particularly, Fe-C nanoparticles have been recently shown as efficient nanocatalyts for magnetically-induced CO_2 hydrogenation [124]. In these applications, where the product fH_{ac} is not limited by human exposure, an efficient increase of the heating capacity could be easily accomplished by the increase in the exciting frequency. The reduction of the mean Fe-C nanoparticle dimensions below or around the monodomain-multidomain critical size (i.e. optimization of the temperature/time reduction annealings) is an effective strategy to enhance the magnetic induction heating capacity. Furthermore, for higher frequencies the eddy current losses in this partial conductive media would also contribute to the magnetic heating enhancement and provide to these nanocomposites promising features to be applied in emergent environmental areas.

4. Discussion

The previous extensive structural and magnetic analysis in these Fe-C nanocomposites enables to outline a final discussion about the main parameters controlling the sugar decomposition and the Fe reduction process. According to the obtained results, it can be concluded that the first stages of the decomposition process can be ascribed to the occurrence of iron oxides as initial precursors. As previously reported [35], the decomposition of carbohydrates in the presence of Fe^{3+} takes place through the initial formation of iron oxide/hydroxide nanoparticles embedded in a carbonaceous matrix (hydrochar) according the following reactions:

$$Fe^{3+} + 3H_2O \rightarrow Fe(OH)_3 + 3H^+ \qquad (3)$$

$$Fe(OH)_3 \rightarrow FeO(OH) + H_2O \rightarrow Fe_2O_3 + H_2O \qquad (4)$$
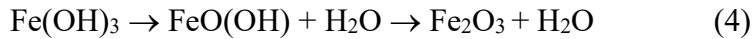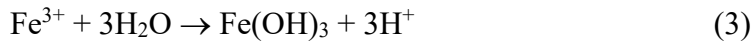
These iron oxide/hydroxide nanoparticles interacts with the first nuclei of the carbonaceous material formed from the carbohydrate (glucose in [35]) decomposition. These oxides chemically react with carbon, leading to the reduced Fe species:

$$6Fe_2O_3 + C \rightarrow 4Fe_3O_4 + O_2 \qquad (5)$$

$$Fe_3O_4 + C \rightarrow 3FeO + CO \qquad (6)$$

$$FeO + CO \rightarrow Fe + CO_2 \qquad (7)$$

In the present case, a complex hydroxide antiferromagnetic phase is detected at the first stages of the decomposition process, where a small fraction of magnetite (Fe_3O_4) can be

also deduced both from X-ray diffraction and the low field magnetization measurements. The occurrence of hematite (α-Fe$_2$O$_3$) can be excluded in the samples, both from the Rietveld X-ray analysis and the magnetic characterization (absence of the Morin transition at $T_m \sim 240$ K). As confirmed by the previous characterizations (FTIR, X-ray diffraction, TEM, Raman spectroscopy and *dc* magnetic characterization) the decomposition process and the final Fe reduction is shifted towards lower annealing temperatures when sucrose is employed as reducing agent. However, the thermogravimetry analysis (TGA, see fig.1) does not show clear differences in the decomposition temperatures of the *P-sugars* samples. However, due to the highest molecular weight of the sucrose (342. 2 g/mol) in comparison with the value of the other sugars (180.16 g/mol), the initial mixture (8 wt. %Fe) would provide a slightly higher % at C/Fe in the sucrose samples (3.78 and 3.57 carbon atoms per Fe atom for the sucrose and fructose or glucose, respectively). The higher C/Fe ratio for the sucrose samples would contribute to speed up the decomposition process, but additional factors (i.e. thermal conductivity of the dried paste) should also be taken into consideration to fully understand the first stages of the decomposition process in these sugars.

Regarding the final stages of the decomposition process, as eq. 7 shows, zero valent Fe is obtained from the final reduction of the Fe oxides by carbon. Nevertheless, as previously discussed, Fe$_3$C is the majority phase obtained in the reduced samples. The formation of iron-carbide particles encapsulated by graphitic layers can be analyzed taking into account the equilibrium iron-phase diagram [85]. This phase diagram for *wt%C* < 10 can be divided in two main regions. For *wt%C* < 6.67, Fe$_3$C (cementite) and α-Fe (ferrite) coexist for $T \leq$ 727°C, while at higher temperatures (T > 727°C) the transformation of α-Fe to γ-Fe takes

place. Due to the low solubility of C in the ferrite phase, only very low carbon contents (0.022 *wt%*C) could be placed interstitially in the bcc Fe phase. Thus, the increase in *wt%*C (as in the sucrose samples) gives rise to the increase in the % of cementite, coexisting with the α-Fe phase. A further increase in *wt%*C (6.67 < *wt%*C < 10), leads to the coexistence of Fe_3C and graphite for $T \leq 1147°C$ (melting temperature of the Fe_3C phase). Therefore, assuming a non-completely homogenous carbon distribution in the reduced samples, the microstructure would contain a small fraction of α-Fe (≤ 5 *wt%*), Fe_3C (11-22 wt%) and a carbon graphite matrix as majority phase (75-89 *wt%*). Furthermore, at annealing temperatures above 727°C (i.e. 800°C), all the ferrite will be in the austenite phase (γ-Fe), coexisting with the cementite Fe_3C phase. Thus, the encapsulation of these nanoparticles by graphitic ordered layers (as the Raman spectroscopy reflects) would promote the stabilization of the γ-Fe phase at room temperature. Quenching of this metastable phase would give rise to the increase in the antiferromagnetic component for samples with a highly ordered carbon state (i.e. A-sucrose800), and thus to the decrease in the experimental high field magnetization.

5. Conclusions

Fe-based carbonaceous nanocomposites have been synthesized by thermal decomposition of sugars (fructose, glucose and sucrose) employing $FeCl_3$ as Fe^{3+} source. The aqueous solution (8 wt. %Fe), was initially dried and subsequently thermally treated under controlled Ar atmosphere (annealing temperatures, 400 to 800°C; 1 hour). An extensive structural analysis (Thermogravimetry (TGA), Infrared (FTR) spectroscopy, X-ray diffractometry, TEM microscopy and Raman spectroscopy) confirms the reduction of Fe^{3+} mediated by the carbon sugar source and the formation of Fe-based nanoparticles surrounded

by a carbon matrix for high annealing temperatures. The encapsulation of the magnetic Fe based nanoparticles by highly ordered graphite layers is clearly visible through HRTEM images and confirmed by the analysis of the carbon order state through Raman spectroscopy. A speed up (shift towards lower annealing temperatures) of the decomposition process is found when sucrose is employed as reduced agent. Thus, Fe based carbonaceous nanocomposites (coexistence of α-Fe (≤ 5 *wt%*), Fe_3C (11-22 wt%) magnetic nnaoparticles surrounded by a majority carbon graphite matrix (75-89 *wt%*)) are obtained for annealing temperatures $T_{ann} = 800°C$ for fructose and glucose samples, and $T_{ann} = 600°C$ in the sample reduced with sucrose. Such a phase distribution and the microstructural evolution under the performed annealing treatments are confirmed by *dc* magnetometry, in particular the temperature evolution (5-300 K) of the high (6 T) and low field (*ZFC-FC* curves at 50 Oe) magnetization. While an antiferromagnetic response (Curie-Weiss law) is found at the initial stages of the decomposition process (occurrence of elongated/needle nanoparticles similar to Fe hydroxides), ferromagnetic behavior (Bloch law) mainly characterizes the samples of the reduced samples at high temperature (ferromagnetic Fe-based nanoparticles). Furthermore, the magnetization process was analyzed through the *ac* hysteresis loops where the phase and nanoparticles size distribution determines the magnetic response of the reduced samples. Thus, nearly anhysteretic large multi-domain α-Fe nanoparticles would slightly contribute to the *ac* magnetic coercivity, being the area of the *ac* hysteresis loops and thus the *SAR* coefficient mainly determined by the smaller Fe_3C nanoparticles. Accordingly, maximum *SAR* values (~ 70 W/g_{Fe}), are found for the fructose sample reduced at $T_{ann} = 800°C$ as a consequence of the lower main grain size. In spite of the moderate *SAR* values obtained, these synthesized nanocomposites display promising properties to be applied in different emerging

fields where the local increase in temperature can enhance and optimize their potential use (i.e. magnetic adsorbers and catalysts, biocompatible nanocomposites for the biomedical field).

References

1.- S. L. Candelaria, Y. Shao, W. Zhu, X. Li, J. Xiao, J-G. Zhang, Y. Wang, J. Liu, J. Li, G. Cao, *Nanostructured carbon for energy storage and conversion*, Nano Energy 1 (2012) 195-220. doi.org/10.1016/j.nanoen.2011.11.006.

2.- W. Gu, G. Yushin*, Review of nanostructured carbon materials for electrochemical capacitor applications: advantages and limitations of activated carbon, carbide‑derived carbon, zeolite‑templated carbon, carbon aerogels, carbon nanotubes, onion‑like carbon, and graphene,* WIREs Energy Environ 3 (2014) 424–473. doi: 10.1002/wene.102.

3.- J. Tang, J. Liu, N. L. Torada, T. Kimura, Y. Yamauchi, *Tailored design of functional nanoporous carbon materials toward fuel cell applications,* Nano Today 9 (2014) 305-323. doi.org/10.1016/j.nantod.2014.05.003

4.- S. Qiu, L. Xiao, M. L. Sushko, K. S. Han, Y. Shao, M. Yan, X. Liang, L. Mai, J. Feng, Y. Cao, X. Ai, H. Yang, J. Li*, Manipulating Adsorption–Insertion Mechanisms in Nanostructured Carbon Materials for High‑Efficiency Sodium Ion Storage,* Adv. Energy Mater., 7 (2017) 1700403. doi.org/10.1002/aenm.201700403.

5.- M. A. Beluomini, J. L. da Silva, A. Cardoso de Sá, E. Buffon, T. C. Pereira, N. R. Stradiotto, *Electrochemical sensors based on molecularly imprinted polymer on nanostructured carbon materials: A review,* J. Electroanal. Chem. 840 (2019) 343-366. doi.org/10.1016/j.jelechem.2019.04.005.

6.- Y. Xu, R. Arrigo, X. Liu, D. Su, *Characterization and use of functionalized carbon nanotubes for the adsorption of heavy metal anions,* New Carbon Mater. 26 (2011) 57-62. doi.org/10.1016/S1872-5805(11)60066-8.

7.- D. Salinas-Torres, M. Navlani-García, K. Mori, Y. Kuwahara, H. Yamashita, *Nitrogen-doped carbon materials as a promising platform toward the efficient catalysis for hydrogen generation,* Appl. Catal. A-gen. 571 (2019) 25-41. doi.org/10.1016/j.apcata.2018.11.034.

8.- Q. Liu, J. Gu, W. Zhang, Y. Miyamoto, Z. Chen, D. Zhang, *Biomorphic porous graphitic carbon for electromagnetic interference shielding*, J. Mater. Chem., 22 (2012) 21183-21188. doi.org/10.1039/C2JM34590K.

9.- B. J.Mapleback, T. J.Simons, Y. Shekibi, K. Ghorbani, A. N. Rider, *Structural composite supercapacitor using carbon nanotube mat electrodes with interspersed metallic iron nanoparticles,* Electrochim. Acta 331 (2020) 135233. doi.org/10.1016/j.electacta.2019.135233.

10.- L. Cao, Q. Luo, W. Liu, Y. Lin, X. Liu, Y. Cao, W. Zhang, Y. Wu, J. Yang, T. Yao, S. Wei, *Identification of single-atom active sites in carbon-based cobalt catalysts*

during electrocatalytic hydrogen evolution, Nat Catal 2 (2019) 134–141. doi.org/10.1038/s41929-018-0203-5.

11. G. Liu, B. Wang, P. Ding, W. Wei, Y. Ye, L. Wang, W. Zhu, H. Li, J. Xi, *In-situ synthesis strategy for CoM (M = Fe, Ni, Cu) bimetallic nanoparticles decorated N-doped 1D carbon nanotubes/3D porous carbon for electrocatalytic oxygen evolution reaction*, J. Alloy. Compd. 815 (2020) 152470, doi.org/10.1016/j.jallcom.2019.152470

12.- A. F. Baye, R. Appiah-Ntiamoah, H. Kim, *Synergism of transition metal (Co, Ni, Fe, Mn) nanoparticles and "active support" Fe3O4@C for catalytic reduction of 4-nitrophenol,* Sci Total Environ 712, 10, (2020) 135492. doi.org/10.1016/j.scitotenv.2019.135492.

13.- J. A. Bobb, F. S. Awad, S. Moussa, M. S. El-Shall, *Laser synthesis of magnetite-partially reduced graphene oxide nanocomposites for arsenate removal from water*, J Mater Sci 55 (2020) 5351–5363. doi.org/10.1007/s10853-020-04363-6.

14.- C. B. Paz, R. S. Araújo, L. F. Oton, A. C. Oliveira, J. M. Soares, S. N. Medeiros, E. Rodríguez-Castellón, E. Rodríguez-Aguado, *Acid red 66 dye removal from aqueous solution by Fe/C-based composites: Adsorption, kinetics and thermodynamic studies,* Materials 13(5) (2020) 1107. doi.org/10.3390/ma13051107.

15.- M. Nodehi, M. Baghayeri, R. Ansari, H. Veisi, *Electrochemical quantification of 17α – Ethinylestradiol in biological samples using Au/Fe₃O₄@TA/MWNT/GCE sensor,* Mater. Chem. Phys. 244 (2020) 122687. doi.org/10.1016/j.matchemphys.2020.122687.

16.- J. Liu, Y. Zhu, X. Li, F. Du, R. Wang, L. Jiang, *Three-dimensional Fe, N-doped carbon nanosheets on interconnected carbon skeletons as a highly efficient and stable electrocatalyst for oxygen reduction reaction,* J. Alloy. Compd. 788 (2019) 1274. doi.org/10.1016/j.jallcom.2019.03.010.

17.- X. Sun, P. Wei, S. Gu, J. Zhang, Z. Jiang, J. Wan, Z. Chen, Li Huang, Yue Xu, Chun Fang, Qing Li, Jiantao Han, Yunhui Huang, *Atomic-Level Fe-N-C Coupled with Fe₃C-Fe Nanocomposites in Carbon Matrixes as High-Efficiency Bifunctional Oxygen Catalysts*, Small 16, 6, (2020) 1906057. doi.org/10.1002/smll.201906057.

18.- Y. S. Lim, C. W. Lai, S. B. A. Hamid, *Porous 3D carbon decorated Fe₃O₄ nanocomposite electrode for highly symmetrical supercapacitor performance,* RSC Adv., 7 (2017) 23030-23040. doi.org/10.1039/C7RA00572E.

19.- C. Wang, S. Mutahir, L. Wang, W. Lei, X. X. Xinyan, J. Qing, L. Hao, *Hierarchical MOF-derived layered Fe₃O₄ QDs@C imbedded on graphene sheets as a high-performance anode for Lithium-ion storage,* Appl. Surf. Sci. 509 (2020) 144882. doi.org/10.1016/j.apsusc.2019.144882.

20.- I. P. Grudzinski, M. Bystrzejewski, P. Bogorodzki, A. Cieszanowski, W. Szeszkowski, M. Poplawska, M. Bamburowicz-Klimkowska, *Comprehensive magnetic*

resonance characteristics of carbon-encapsulated iron nanoparticles: a new frontier for the core-shell–type contrast agents, J Nanopart Res 22 82 (2020) 82. https://doi.org/10.1007/s11051-020-04795-w

21.- A. Tiwari, N.C. Verma, S. Turkkan, A. Debnath, A. Singh, G. Draeger, C. K. Nandi, J. K. Randhawa, *Graphitic Carbon Coated Magnetite Nanoparticles for Dual Mode Imaging and Hyperthermia,* ACS Appl. Nano Mater. 3, 1 (2020) 896-904. doi.org/10.1021/acsanm.9b02501.

22.- K. Wang, Y. Chen, H. Li, B. Chen, K. Zeng, Y. Chen, H. Chen, Q. Liu, and H. Liu, *Fe/N-Codoped Hollow Carbonaceous Nanospheres Anchored on Reduced Graphene Oxide for Microwave Absorption,* ACS Appl. Nano Mater. 2 (12), (2019) 8063-8074. DOI: 10.1021/acsanm.9b02192.

23.-, L. Wang, H. Xiong, S. Ur Rehman, Y. Chen, Q. Tan, L. Zhang, M. Zhong, Z. Zhong *Optimized microstructure and impedance matching for improving the absorbing properties of core-shell C@Fe₃C/Fe nanocomposites,* J. Alloy. Compd. 780 (2019) 552 doi.org/10.1016/j.jallcom.2018.12.001.

24.- H. Sun, G. Zhou, S. Liu, H. M.Ang, M. O Tadé, S. Wang, *Nano-Fe0 Encapsulated in Microcarbon Spheres: Synthesis, Characterization, and Environmental Applications,* ACS Appl. Mater. Interfaces 4, 11 (2012) 6235-6241. doi.org/10.1021/am301829u.

25.- J. Zhang, Z. Cheng, X. Yang, J. Luo, H. Li, H. Chen, Q. Zhang, J. Li, *Mediating the reactivity and selectivity of nanoscale zerovalent iron toward nitrobenzene under porous carbon confinement,* Chem. Eng. J 393 (2020) 124779.

26.- N. Zhou, K. Gong, Q. Hu, X. Cheng, J. Zhou, M. Dong, N.Wang, T. Ding, B. Qiu, Z. Guo, *Optimizing nanocarbon shell in zero-valent iron nanoparticles for improved electron utilization in Cr(VI) reduction,* Chemosphere 242, (2020) 125235. doi.org/10.1016/j.chemosphere.2019.125235.

27.- S. Xiao, H. Ma, M. Shen, S. Wang, Q. Huang, X. Shi, *Excellent copper(II) removal using zero-valent iron nanoparticle-immobilized hybrid electrospun polymer nanofibrous mats,* Colloid Surface A, 381, 1–3, 20 (2011) 48-54.

28.- A. Mitzia, M. Vítková, M. Komárek, *Assessment of biochar and/or nano zero-valent iron for the stabilisation of Zn, Pb and Cd: A temporal study of solid phase geochemistry under changing soil conditions,* Chemosphere 242 (2020) 125248. doi.org/10.1016/j.chemosphere.2019.125248.

29.- A. Goswami, R. G. Kadam, J. Tuček, Z. Sofer, D. Bouša, R. S. Varmaa, M. B. Gawande, R. Zbořil, *Fe(0)-embedded thermally reduced graphene oxide as efficient nanocatalyst for reduction of nitro compounds to amines,* Chem. Eng. J 382, 15 (2020) 122469. doi.org/10.1016/j.cej.2019.122469.

30.- Q. Long, F. Liu, Y. Yuan, Y. Dai, C. Wang, X. Li, J. Zhang, *Enhanced degradation performance of p-chlorophenol in photo-Fenton reaction activated by nano-Fe^0 encapsulated in hydrothermal carbon: Improved Fe(III)/Fe(II) cycle,* Colloid Surface A, 594 (2020) 124650. doi.org/10.1016/j.colsurfa.2020.124650.

31.- M. Gu, Q. Sui, U. Farooq, X. Zhang, Z. Qiu, S. Lyu, *Enhanced degradation of trichloroethylene in oxidative environment by nZVI/PDA functionalized rGO catalyst,* J. Hazard. Mater 359, 5 (2018) 157-165. doi.org/10.1016/j.jhazmat.2018.07.013.

32.- X. Chen, X. Lv, Q. Yang, Y. Wang, X. Jin, J. Wang, Z. Yang, *Dechlorination of carbon tetrachloride by Nanoscale Nickeled Zero-Valent Iron @ Multi-Walled Carbon Nanotubes: Impact of reaction conditions, kinetics and mechanism,* Appl. Organomet. Chem. 33, 3(2019) e4772. doi.org/10.1002/aoc.4772.

33.- H. Sun, G. Zhou, S. Liu, H. M. Ang, M. O Tadé, S. Wang, *Nano-Fe0 Encapsulated in Microcarbon Spheres: Synthesis, Characterization, and Environmental Applications*, ACS Appl. Mater. Interfaces 4, 11 (2012) 6235-6241. doi.org/10.1021/am301829u.

34.- Z. Li, Y. Sun, Y. Yang, Y. Han, T. Wang, J. Chen, D. C. W.Tsang, *Biochar-supported nanoscale zero-valent iron as an efficient catalyst for organic degradation in groundwater,* J. Hazard. Mater. 383, 5 (2020) 121240.

35.- L. H. SousaVieira, C. M. Sganzerla Sabino, F. H. Soares Júnior, J. S. Rocha, M. Oliveira Castro, R. Silva Alencar, L. Souza da Costa, B. Cruz Viana, A. Jardim de Paula, J. M. Soares. A. Gomes Souza Filho, L. Otubo, P. B. Almeida Fechine, A. Ghosh, O. Pastor Ferreira, *Strategic design of magnetic carbonaceous nanocomposites and its application as multifunctional adsorbent,* Carbon 161 (2020) 758-771. doi.org/10.1016/j.carbon.2020.01.089.

36.-H. Lyu, J. Tang, M. Cui, B. Gao, B. Shen*, Biochar/iron (BC/Fe) composites for soil and groundwater remediation: Synthesis, applications, and mechanisms,* Chemosphere 246 (2020) 125609.doi.org/10.1016/j.chemosphere.2019.125609.

37.- X. Liu, L. Yang, H. Zhao, W. Wang, *Pyrolytic production of zerovalent iron nanoparticles supported on rice husk-derived biochar: simple, in situ synthesis and use for remediation of Cr(VI)-polluted soils*, Sci Total Environ 708, 15 (2020) 134479. doi.org/10.1016/j.scitotenv.2019.134479.

38.- S. Li, T. You, Y. Guo, S. Yao, S. Zang, M. Xiao, Z. Zhang, Y. Shend, *High dispersions of nano zero valent iron supported on biochar by one-step carbothermal synthesis and its application in chromate removal,* RSC Adv. 9 (2019) 12428-12435. doi.org/10.1039/C9RA00304E.

39.- J. Zhang, Z. Cheng, X. Yang, J. Luo, H. Li, H. Chen, Q. Zhang, J. Li, *Mediating the reactivity and selectivity of nanoscale zerovalent iron toward nitrobenzene under porous carbon confinement,* Chem. Eng J 393 (2020) 124779..

40.- F. M. Abel, S. Pourmiri, G. Basina, V. Tzitzios, E. Devlinc, G. C. Hadjipanayisa, *Iron carbide nanoplatelets: colloidal synthesis and characterization,* Nanoscale Adv.,1 (2019) 4476-4480. doi.org/10.1039/C9NA00526A.

41.- M. Amiri, M. Salavati-Niasari, A. Akbari, *Magnetic nanocarriers: Evolution of spinel ferrites for medical applications,* Adv. Colloid. Interfac. 265 (2019) 29-44. doi.org/10.1016/j.cis.2019.01.003.

42.- N. Ž. Knežević, I. Gadjanski, J. Durand, *Magnetic nanoarchitectures for cancer sensing, imaging and therapy,* J. Mater. Chem. B, 7 (2019) 9-23. doi.org/10.1039/C8TB02741B.

43.- X. Han, K. Xu, O. Taratula, K. Farsad, *Applications of nanoparticles in biomedical imaging*, Nanoscale, 11 (2019) 799-819. doi.org/10.1039/C8NR07769J.

44.- J. Gao, H. Gu, B. Xu, *Multifunctional Magnetic Nanoparticles: Design, Synthesis, and Biomedical Applications*, Acc. Chem. Res. 42, 8 (2009) 1097-1107. doi.org/10.1021/ar9000026.

45.- P. Tartaj, M. P. Morales, S. Veintemillas-Verdaguer, T. González-Carreño, C. J Serna, *The preparation of magnetic nanoparticles for applications in biomedicine, J.* Phys. D: Appl. Phys. 36 (2013) R182. doi.org/10.1088/0022-3727/36/13/202.

46.- C. Xu, S. Sun, *New forms of superparamagnetic nanoparticles for biomedical applications,* Adv. Drug Deliv. Rev. 65, 5 (2013) 732-743. doi.org/10.1016/j.addr.2012.10.0.

47.- S. Zhou, Y. Li, F. Cui, M. Jia, X. Yang, Y. Wang, L. Xie, Q. Zhang, Z. Hou, *Development of multifunctional folate-poly(ethylene glycol)-chitosan-coated Fe_3O_4 nanoparticles for biomedical applications,* Macromol. Res. 22 (2014) 58–66. doi.org/10.1007/s13233-014-2008-y.

48.- Y. Hu, J. Li, J. Yang, P. Wei, Y. Luo, L. Ding, W. Sun, G. Zhang, X. Shi, Mingwu Shen, *Facile synthesis of RGD peptide-modified iron oxide nanoparticles with ultrahigh relaxivity for targeted MR imaging of tumors,* Biomater. Sci.,3 (2015) 721-732. doi.org/10.1039/C5BM00037H.

49.- M. Sonmez, M. Georgescu, L. Alexandrescu, D. Gurau, A. Ficai, D. Ficai, E. Andronescu, *Synthesis and applications of Fe_3O_4/SiO_2 core-shell materials,* Curr. Pharm. Des. 2, 37 (2015) 5324 – 5335. 10.2174/1381612821666150917094031.

50.- T. Ogawa1, K. Seto, D. Hasegawa, H. T. Yang, H. Kura, M. Doi, M. Takahashi, *Effect of Nucleation and Growth Dynamics on Saturation Magnetization of Chemically Synthesized Fe Nanoparticles,* J. Magn. 16, 3 (2011) 308-311. dx.doi.org/10.4283/JMAG.2011.16.3.308.

51.- P. Guardia, B. Batlle-Brugal, A.G. Roca, O. Iglesias, M.P. Morales, C.J. Serna, A. Labarta, X. Batlle, *Surfactant effects in magnetite nanoparticles of controlled size*, J. Mag. Mag. Mat., 316, 2 (2007) e756-e759. doi.org/10.1016/j.jmmm.2007.03.085.

52.- P. Z. Si, Z. D. Zhang, D.Y. Geng, C. Y. You, X. G. Zhao, W. S. Zhang, *Synthesis and characteristics of carbon-coated iron and nickel nanocapsules produced by arc discharge in ethanol vapor,* Carbon 4, 2 (2003) 247-251. doi.org/10.1016/S0008-6223(02)00280-4.

53.- Z. Abdullaeva, E. Omurzak, C. Iwamoto, H. S. Ganapathy, S. Sulaimankulova, C. Liliang, T. Mashimo, *Onion-like carbon-encapsulated Co, Ni, and Fe magnetic nanoparticles with low cytotoxicity synthesized by a pulsed plasma in a liquid,* Carbon 50, 5, (2012) 1776-1785. doi.org/10.1016/j.carbon.2011.12.025.

54.- A.A. El-Gendy, E.M.M Ibrahim, V.O. Khavrus, Y. Krupskaya, S. Hampel, A. Leonhardt, B.Büchner, R.Klingeler, *The synthesis of carbon coated Fe, Co and Ni nanoparticles and an examination of their magnetic properties,* Carbon 47, 12 (2009) 2821-2828. doi.org/10.1016/j.carbon.2009.06.025.

55.- F. Dumestre, B. Chaudret, C. Amiens, P. Renaud, P. Fejes, *Superlattices of Iron Nanocubes Synthesized from Fe[N(SiMe₃)₂]₂,* Science, 303, 565906 (2004). 821-823. 10.1126/science.1092641.

56.- L. M. Lacroix, N. Frey Huls, D. Ho, X. Sun, K. Cheng, S. Sun, *Stable Single-Crystalline Body Centered Cubic Fe Nanoparticles*, Nano Lett. 11, 4 (2011) 1641-1645. doi.org/10.1021/nl200110t.

57.- Z. Schnepp, S. C. Wimbush, M. Antonietti, C. Giordano, *Synthesis of Highly Magnetic Iron Carbide Nanoparticles via a Biopolymer Route*, Chem. Mater. 22, 18 (2010) 5340-5344. doi.org/10.1021/cm101746z.

58.- A. Gangwara, S.S. Varghesea, Sher Singh Meenab, C.L. Prajapatc, N. Guptac, N.K. Prasada, *Fe₃C nanoparticles for magnetic hyperthermia application,* J. Magn. Magn. Mat. 481 (2019) 251-256. doi.org/10.1016/j.jmmm.2019.03.028.

59.- E. P. Sajitha, V. Prasad, S. V. Subramanyam, A. K. Mishra, S. Sarkar, C.Bansal, *Structural, magnetic and Mössbauer studies of iron inclusions in a carbon matrix*, J. Magn. Magn. Mat. 313, 2 (2007) 329-336. doi.org/10.1016/j.jmmm.2007.02.001.

60.- M. M. Saiq, K. Suzuki, M. R. Hill, *Towards energy efficient separations with metal organic frameworks*, Chem. Commun. 54 (2018) 2825-2837. doi.org/10.1039/C8CC00331A.

61.- L. Melag, M. M. Sadiq, S. J. D. Smith, K. Konstas, K. Suzuki, M. R. Hill *Efficient delivery of oxygen via magnetic framework composites*, J. Mater. Chem. A 7 (2019) 3790-3796. doi.org/10.1039/C8TA07739H.

62.- C. Gómez-Polo, S. Larumbe, L.F. Barquín, L.R. Fernández, *Magnetic induction heating as a new tool for the synthesis of Fe3O₄–TiO₂ nanoparticle systems*, J. Nanopart. Res. 18 (2016) 118. doi.org/10.1007/s11051-016-3426-x.

63.- Y. Tao, G. Huang, H. Li, Matthew R. Hill, *Magnetic metal-organic framework composites:solvent-free synthesis and regeneration driven by localized magnetic induction heat*, ACS Sustain. Chem. Eng. 7 (2019) 13627-13632. doi.org/10.1021/acssuschemeng.9b02323.

64.- C. C. Corten, M. W. Urban, *Repairing polymers using an oscillating magnetic field*, Adv. Mater. 21 (2009) 5011-5015. doi.org/10.1002/adma.200901940

65.- J. Huang, L. Cao, D. Yuan, Y. Chen, *Design of novel self-healing thermoplastic vulcanizates utilizing thermal/magnetic/light-triggered shape memory effects*, ACS Appl. Mater. Interfaces 10 (2018) 40996-41002.

66.- R. Panigrahi, M. Zarek, V. Sharma, D. Cohn Raju, V. Ramanujan, *Bio-inspired multiple cycle healing and damage sensing in elastomer-magnet nanocomposites*, Macromolecular Chem. Phys. 220 (2019) 1900168. doi.org/10.1002/macp.201900168.

67.- Y. Yang, J. He, Q. Li, L. Gao, J. Hu, R. Zeng, J. Qin, S. X. Wang, Q. Wang, *Self-healing of electrical damage in polymers using superparamagnetic nanoparticles*, Nature Nanotech. 14 (2019) 151-155. doi.org/10.1038/s41565-018-0327-4.

68.- J. Moriceau, P. Houizot, M. Pasturel, T. Guizouarn, T. Rouxel, *A magnetic glass matrix (ZnO-BaO-B2O3) particulate (Fe3O4) nanocomposite obtained by SPS*, J. Non-Cryst. Solids 514 (2019) 116-121. doi.org/10.1016/j.jnoncrysol.2019.03.028.

69.- S. H. Vattathurvalappil, M. Ha, *Thermomechanical characterization of nano-$_{Fe3O4}$ reinforced thermoplastic adhesives and single lap-joints*, Compos. Pt. B-Eng. 175 (2019) 107162. doi.org/10.1016/j.compositesb.2019.107162.

70.- S. Salimi, T. S. Babra, G. S. Dines, S. W. Baskerville, W. Hayes, B. W. Greenland, *Composite polyurethane adhesives that debond-on-demand by hysteresis heating in an oscillating magnetic field,* Eur. Polym. J. 121 (2019) 109264. doi.org/10.1016/j.eurpolymj.2019.109264.

71.-P. Mølgaard Mortensen, J. Soland Engbæk, S. Bastholm Vendelbo, M. Fougt Hansen, *Direct hysteresis heating catalytically active Ni-Co nanoparticles as stem reforming catalysts*, Ind. Eng. Chem. Res. 56 (2017) 14006-14013. doi.org/10.1021/acs.iecr.7b02331

72.- J. M. Asensio, A. B. Miguel, P. F. Fazzini, P. W. N. M. van Leeuwen, B. Chaudret*, Hydrodeoxygenation using magnetic induction: high-temperature heterogeneous catalysis in solution*, Angew. Chem. 58, 33 (2019) 11306-11310. doi.org/10.1002/anie.201904366.

73.- F. Varsano, M. Bellusci, A. La Barbera, M. Petrecca, M. Albino, C. Sangregorio, *Dry reforming of methane powered by magnetic induction*, Int. J. Hydrog. Energy 44, 38, (2019) 21037-21044. doi.org/10.1016/j.ijhydene.2019.02.055.

74.- D. De Masi, J. M. Asensio, P. F. Fazzini, L. M. Lacroix, B. Chaudret, *Engineering Iron–Nickel Nanoparticles for Magnetically Induced CO_2 Methanation in Continuous Flow,* Angew. Chem. 59, 15 (2020) 6187-6191doi.org/10.1002/anie.201913865.

75.- M. R. Almind, S. Bastholm Vendelbo, M. Fougt Hansen, M. Gotthold Vinum, C. Frandsen, P. Mølgaard Mortensen, J. Soland Engbæk, *Improving performance of induction-heated steam methane reforming*, Catal. Today, 342 (2020) 13-20. doi.org/10.1016/j.cattod.2019.05.005.

76.- F. L. Rivera, F. J. Palomares, P. Herrasti, E. Mazario, *Improvement in heavy metal removal from wastewater using an external magnetic inductor*, Nanomaterials 9 (2019) 1508. doi.org/10.3390/nano9111508

77- J. Rodriguez-Carvajal, *Recent advances in magnetic structure determination by neutron powder diffraction*, Physica B 192 (1993) 55. doi.org/10.1016/0921-4526(93)90108-I.

78- E. Garaio, J. M. Collantes, F. Plazaola, J. A. García, I. Castellanos-Rubio, *A multifrequency electromagnetic applicator with an integrated AC magnetometer for magnetic hyperthermia experiments*, Meas. Sci. Technol 25 (2014) 10.1088/0957-0233/25/11/115702

79.- M.I. Abd-Elrahman, S.M. Ahmed, *Thermal degradation kinetics and geometrical stability of D-sucrose*, Int. J. Polym. Mater, 58 (2009) 322-335. doi.org/10.1080/00914030902859273.

80.- M. Hurtta, Ilkka P. J. Knuutinen, *Melting behavior of D-sucrose, D-glucose and D-fructose*, Carbohydr. Res. 339 (2004) 2267-2273. doi.org/10.1016/j.carres.2004.06.022.

81.- K. Lotz, A. Wütscher, H. Düdder, C. M. Berger, C. Russo, K. Mukherjee, G. Schwaab, M. Havenith, M. Muhler, *Tuning the Properties of Iron-Doped Porous Graphitic Carbon Synthesized by Hydrothermal Carbonization of Cellulose and Subsequent Pyrolysis,* ACS Omega 4, 2 (2019) 4448-4460. doi.org/10.1021/acsomega.8b03369.

82.- A. Henry, P. Hesemann, J. G. Alauzun, B. Boury, *Reductive mineralization of cellulose with vanadium, iron and tungsten chlorides and access to M_xO_y metal oxides and M_xO_y/C metal oxide/carbon composites,* Carbohydr. Polym. 174, 15 (2017) 697-705. doi.org/10.1016/j.carbpol.2017.06.106.

83.- Z. Pan, Y. Lin, B. Sarkar, G. Owens, Z. Chen, *Green synthesis of iron nanoparticles using red peanut skin extract: Synthesis mechanism, characterization and effect of conditions on chromium removal,* J. Colloid Interface Sci 558, 15 (2020) 106-114. oi.org/10.1016/j.jcis.2019.09.106.

84.- H.Y. Xu, B. Li, T.-N. Shi, Y. Wang, S. Komarneni*, Nanoparticles of magnetite anchored onto few-layer graphene: A highly efficient Fenton-like nanocomposite catalysts*, J. Colloid Interface Sci, 532 (2018) 161-170.

85.- S. T. Neeli, H. Ramsurn, *Synthesis and formation mechanism of iron nanoparticles in graphitized carbon matrices using biochar from biomass model compounds as a support,* Carbon 134 (2018) 480-490. doi.org/10.1016/j.carbon.2018.03.079.

86.- R. Kumar, A. Kumar, N. Verma, A. V. Anupama, R. Philip, B. Sahoo, *Modulating non-linear optical absorption through controlled graphitization of carbon nanostructures containing Fe₃C-graphite core-shell nanoparticles,* Carbon 153 (2019) 545-556. doi.org/10.1016/j.carbon.2019.07.058.

87.- O. Hassel, H. Mark, *Über die Kristallstruktur des Graphit*s, Z. Physik 25 (1924) 317–337. doi.org/10.1007/BF01327534.

88.- H. I. Faraoun, Y. D. Zhang, C. Esling, H. Aourag, *Crystalline, electronic, and magnetic structures of θ-Fe₃C, χ-Fe₅C₂, and η-Fe₂C from first principle calculation*, J. Appl. Phys. 99, 093508 (2006); https://doi.org/10.1063/1.2194118

89.- A. Sutton, W. Hume-Rothery, *The lattice spacings of solid solutions of titanium, vanadium, chromium, manganese, cobalt and nickel in α-iron*, Philos. Mag, vol. 46, pp. 1295-1309, 1955.

90.- C. M. Hansel, S. G. Benner, S.t Fendorf, *Competing Fe(II)-Induced Mineralization Pathways of Ferrihydrite,* Environ. Sci. Technol., 39, 18, (2005) 7147-7153. doi.org/10.1021/es050666z.

91.- S. W. Bokhari, H. Pan, A. H. Siddique, M. Imtiaz, Z. Chen, Y. Li, S. Zhu, *Self-assembly of β-FeOOH/rGO/CNT for a high-performance supercapacitor*, Mater. Lett. 220, 1 (2018) 140-143. doi.org/10.1016/j.matlet.2018.02.131.

92.- M. A. Pimenta, G. Dresselhaus, M. S. Dresselhaus, L. G. Cançado, A. Jorio, R. Saito, *Studying disorder in graphite-based systems by Raman spectroscopy*, Phys. Chem. Chem. Phys., 2007,9, 1276-1290. doi.org/10.1039/B613962K.

93.- N. Soin, S. Sinh Roy, T. H. Lim, J. A. D. McLaughlin, *Microstructural and electrochemical properties of vertically aligned few layered graphene (FLG) nanoflakes and their application in methanol oxidation,* Mater. Chem. Phys, 129 (2011) 1051-1057. doi.org/10.1016/j.matchemphys.2011.05.063.

94.-, L. Bokobza, J. L. Bruneel, M. Couzi, *Raman spectra of carbon-based materials (from graphite to carbon black) and of some silicone composites*, C, 1 (2015) 77-94. doi.org/10.3390/c1010077

95.- A. Gupta, G. Chen, P. Joshi, S. Tadigadapa, P.C. Eklund, *Raman Spectra of Carbon-Based Materials (from Graphite to Carbon Black) and of Some Silicone Composites,* Nano Lett. 6, 12 (2006) 2667-2673. doi.org/10.1021/nl061420a.

96.- Y. Wang, S. Liu, P. Huang, H. Xie, X. Qiao, *Structural and magnetic properties of mono-dispersed iron carbide (Fe$_x$C$_y$) nanoparticles by facile gas phase reaction*, Ceramics Int. 45 (2019) 11119-11124.

97.- P. Puech, J. M. Plewa, P. Mallet-Ladeira, M. Monthioux, *Spatial confinement model applied to phonons in disordered graphene-based carbons,* Carbon 105 (2016) 275-281. doi.org/10.1016/j.carbon.2016.04.048.

98.- S. Santangelo, G. Messina, G. Faggio, M. Lanza, C. Milone, *Evaluation of crystalline perfection degree of multi-walled carbón nanotubes: correlations between thermal kinetic analysis and micro-Raman spectroscopy*, J. Raman Spectrosc. 42 (2011) 593-602. doi.org/10.1002/jrs.2766.

99.- L. de Bianco, A. Hernando, D. Fiorani, *Exchange Coupling in Iron and Iron/Oxide Nanogranular Systems in Surface Effects of Magnetic Nanoparticles*, Ed. D. Fiorani, Springer (2005) p. 217. ISBN 978-0-387-26018-1.

100.- M, Solzi, F, Cugini, N, Sarzi Amadé, C, Frigeri, G, Attolini, N. N. Musayeva, A. B. Huseynov, S. H. Abdullayeva, C. A. Sultanov, *High-temperature magnetic coercivity of CNTs filled with multi-phase Fe-based nanoparticles,* J. Magn. Magn. Mater. 496, 15 (2020) 165917.

101.- C. Vázquez-Vázquez, M.A. López-Quintela, M.C. Buján-Núñez, J. Rivas *Finite size and surface effects on the magnetic properties of cobalt ferrite nanoparticles*. J. Nanopart. Res. 13 (2011) 1663-1676. doi: 10.1007/s11051-010-9920-7.

102.- S. V. Komogortseva, R. S. Iskhakova, A. D. Balaeva, A. G. Kudashovb,A. V. Okotrubb, S. I. Smirnov, *Magnetic Properties of Fe₃C Ferromagnetic Nanoparticles Encapsulated in Carbon Nanotubes,* Phys. Solid State 49 (2007) 734–738 https://doi.org/10.1134/S1063783407040233.

103.- S. Larumbe, J. I. Pérez-Landazábal, J. M. Pastor, and C. Gómez-Polo, *Sol-gel NiFe₂O₄ nanoparticles: Effect of the silica coating*, J. Appl. Phys. 111, (2012) 103911. doi.org/10.1063/1.4720079.

104.- X. Qi, J. Xu, W. Zhong, Y. Du, *A facile route to synthesize core/shell structured carbon/magnetic nanoparticles hybrid and their magnetic properties,* Mater. Res. Bull., 67 (2015) 162-169.doi.org/10.1016/j.materresbull.2015.03.027.

105.- M. P. Fernández-García, P. Gorria, J. A. Blanco, A. B. Fuertes, M. Sevilla, R. Boada, J. Chaboy, D. Schmool, J. M. Grenèche, *Microstructure and magnetism of nanoparticles with γ-Fe core surrounded by α-Fe and iron oxide shells*, Phys. Rev. B 81 (2010) 094418. doi.org/10.1103/PhysRevB.81.094418

106.- S. Hampel, A. Leonhardt, D. Selbmann, K. Biedermann, D. Elefant, C. Müller, T. Gemming, B. Büchner, *Growth and characterization of filled carbon nanotubes with ferromagnetic properties,* Carbon 44, 11 (2006) 2316-2322. doi.org/10.1016/j.carbon.2006.02.015.

107.- A. Khasanov, J. He, J. Gaillard, K. Yang, A. M. Rao, C. M. Cameron, J. M. Schmeltzer, J. G. Stevens, A. Nath, *The role of γ-iron nanoparticulates in the growth of carbon nanotubes,* Appl. Phys. Lett. 93 (2008) 013103. doi.org/10.1063/1.293712593.

108.- B. Semenenko, P. D. Esquinazi, *Diamagnetism of Bulk Graphite Revised,* Magnetochemistry, 4 (2018) 52. doi:10.3390/magnetochemistry4040052

109.- B. David, O. Schneeweiss, N. Pizúrová, F. Dumitrache, C. Fleaca, R. Alexandrescu, *Nanopowders with superparamagnetic Fe_3C particles and their annealing behavior*, Surf. Interface Anal, 42, 6-7 (2010) 699-702.doi.org/10.1002/sia.3389.

110.- F. Bødker, S. Mørup, M. S. Pedersen, P. Svedlindh, G. T. Jonsson, J. L. Garcia-Palacios, F. J. Lazaro, *Superparamagnetic relaxation in α-Fe particles*, J. Magn. Magn. Mater. 177–181, (1998) 925-927. doi.org/10.1016/S0304-8853(97)00782-8.

111.- G. Barrera, P. Tiberto, C. Sciancalepore, M. Messori, F. Bondioli, P. Allia . *Verwey transition temperature distribution in magnetic nanocomposites containing polydisperse magnetite nanoparticles*. J Mater Sci 54 (2019) 8346–8360. doi.org/10.1007/s10853-019-03510-y.

112.- C. Blanco-Andujar, F. J. Teran, D. Ortega, in *Iron Oxide Nanoparticles for Biomedical Applications* (Eds: M. Mahmoudi, S. Laurent), Elsevier, Amsterdam 2018, p. 197.
113.- J. Carrey, B. Mehdaoui, M. Respaud, *Simple models for dynamic hysteresis loop calculations of magnetic single-domain nanoparticles: Application to magnetic hyperthermia optimization,* J. Appl. Phys. 109 (2011) 083921. doi.org/10.1063/1.3551582.

114.- B. Mehdaoui, A. Meffre, J. Carrey, S. Lachaize, L. M. Lacroix, M. Gougeon, B. Chaudret, M. Respaud, *Optimal Size of Nanoparticles for Magnetic Hyperthermia: A Combined Theoretical and Experimental Study*, Adv. Funct. Mater. 21, 23 (2011) 4573-4581. doi.org/10.1002/adfm.201101243.

115.- D. Gandia, L. Gandarias, I. Rodrigo, J. Robles-García, R. Das, E. Garaio, J. Á. García, M. H. Phan, H. Srikanth, I. Orue, J. Alonso, A. Muela, M. L. Fdez-Gubieda, *Unlocking the potential of magnetotactic bacteria as magnetic hyperthermia agents,* Small 15 (2019) 1902626. doi.org/10.1002/smll.201902626.

116.- A. Kákay, L. K. Varga, *Monodomain critical radius for soft-magnetic fine particles*, J. Appl. Phys. 97 (2005) 083901. doi.org/10.1063/1.1844612.

117.- S. Yamamoto, T. Terai, T. Fukuda, K. Sato, T. Kakeshita, S. Horii, M. Ito, M. Yonemura, *Magnetocrystalline anisotropy of cementite pseudo single crystal fabricated under a rotating magnetic* field, J. Mag. Mag. Mater. 451, 1 (2018) 1-4. doi.org/10.1016/j.jmmm.2017.10.114.

118.- A. Meffre, B. Mehdaoui, V. Kelsen, P. F. Fazzini, J. Carrey, S. Lachaize, M. Respaud, B. Chaudret, *A Simple Chemical Route toward Monodisperse Iron Carbide Nanoparticles Displaying Tunable Magnetic and Unprecedented Hyperthermia Properties,* Nano Lett. 12, 9 (2012) 4722-4728. doi.org/10.1021/nl302160d.

119.- Al. Bordet, R. F. Landis, Y. W. Lee, G. Y. Tonga, J. M. Asensio, C. H. Li, P. F. Fazzini, K. Soulantica, V. M. Rotello, B. Chaudret, *Water-Dispersible and Biocompatible Iron Carbide Nanoparticles with High Specific Absorption Rate,* ACS Nano, 13, 3 (2019) 2870-2878. doi.org/10.1021/acsnano.8b05671.

120.- Q. Li C. W. Kartikowat, S. Horie, T. Iwaki, K. Okuyama, *Correlation between particle size/ domain structure and magnetic properties of highly crystalline Fe_3O_4 nanoparticles*, Sci. Rep. 7 (2017). 10.1038/s41598-017-09897-5

121.- A. R. Muxworthy, W. Williams, *Critical single-domain grain sizes in elongated iron particles: implications for meteoritic and lunar magnetism*, Geophys. J. Int. 202 (2015). 10.1093/gji/ggv180

122.- N. A. Usov O. N. Serebryakova, V. P. Tarasov, I*nteraction Effects in Assembly of Magnetic Nanoparticles*, Nanoscale Res. Lett. 12 (2017). 10.1186/s11671-017-2263-x

123.- R. Hergt, S. Dutz, *Magnetic particle hyperthermia-biophysical limitations of a visionary tumour therapy,* J. Magn. Magn. Mat. 311, 1 (2007) 187-192. 10.1016/j.jmmm.2006.10.1156.

124.- S. S. Kale, J. M. Asensio, M. Estrader, M. Werner, A. Bordet, D. Yi, J. Marbaix, P. F. Fazzini, K. Soulantica, B. Chaudret*, Iron carbide or iron carbide/cobalt nanoparticles for magnetically-induced CO_2 hydrogenation over Ni/SiRAlOx catalysts*, Catal. Sci. Technol., 9 (2019) 2601-2607. doi.org/10.1039/C9CY00437H.